

1
2 **Sensory neuron population expansion enhances odor tracking**
3 **without sensitizing projection neurons**
4
5
6

7 Suguru Takagi^{1,11,*}, Gizem Sancer^{2,12}, Liliane Abuin^{1,12}, S. David Stupski^{3,12}, J.
8 Roman Arguello^{1,4,5,7}, Lucía L. Prieto-Godino^{1,6}, David L. Stern⁷, Steeve Cruchet¹,
9 Raquel Álvarez-Ocaña¹, Carl F. R. Wienecke^{8,9}, Floris van Breugel³, James M.
10 Jeanne², Thomas O. Auer^{1,10,11,13,*} and Richard Benton^{1,13,*}
11

12 ¹Center for Integrative Genomics, Faculty of Biology and Medicine, University of
13 Lausanne, Lausanne, Switzerland
14

15 ²Department of Neuroscience, Yale University, New Haven, Connecticut, USA
16

17 ³Department of Mechanical Engineering, University of Nevada, Reno, Nevada,
18 USA
19

20 ⁴Department of Ecology and Evolution, Faculty of Biology and Medicine,
21 University of Lausanne, Lausanne, Switzerland
22

23 ⁵Swiss Institute of Bioinformatics, Lausanne, Switzerland
24

25 ⁶The Francis Crick Institute, London, UK
26

27 ⁷Janelia Research Campus of the Howard Hughes Medical Institute, Ashburn,
28 Virginia, USA
29

30 ⁸Department of Neurobiology, Stanford University, Stanford, California, USA
31

32 ⁹Present address: Department of Neurobiology, Harvard Medical School,
33 Cambridge, Massachusetts, USA
34

35 ¹⁰Present address: Department of Biology, University of Fribourg, Fribourg,
36 Switzerland
37

38
39 ¹¹These authors contributed equally to this work

40 ¹²These authors contributed equally to this work

41 ¹³Joint senior authors
42

43 *Corresponding authors:

44 Suguru.Takagi@unil.ch

45 Thomas.Auer@unifr.ch

46 Richard.Benton@unil.ch
47
48
49
50

51 **Summary**

52

53 The evolutionary expansion of sensory neuron populations detecting important
54 environmental cues is widespread, but functionally enigmatic. We investigated
55 this phenomenon through comparison of homologous neural pathways of
56 *Drosophila melanogaster* and its close relative *Drosophila sechellia*, an extreme
57 specialist for *Morinda citrifolia* noni fruit. *D. sechellia* has evolved species-specific
58 expansions in select, noni-detecting olfactory sensory neuron (OSN) populations,
59 through multigenic changes. Activation and inhibition of defined proportions of
60 neurons demonstrate that OSN population increases contribute to stronger, more
61 persistent, noni-odor tracking behavior. These sensory neuron expansions result
62 in increased synaptic connections with their projection neuron (PN) partners,
63 which are conserved in number between species. Surprisingly, having more
64 OSNs does not lead to greater odor-evoked PN sensitivity or reliability. Rather,
65 pathways with increased sensory pooling exhibit reduced PN adaptation, likely
66 through weakened lateral inhibition. Our work reveals an unexpected functional
67 impact of sensory neuron expansions to explain ecologically-relevant, species-
68 specific behavior.

69

70 **Introduction**

71

72 Brains display incredible diversity in neuron number between animal species
73 (Godfrey and Gronenberg, 2019; Herculano-Houzel, 2011; Williams and Herrup,
74 1988). Increases in the number of neurons during evolution occur not only
75 through the emergence of new cell types but also through expansion of pre-
76 existing neuronal populations (Arendt et al., 2019; Roberts et al., 2022). Of the
77 latter phenomenon, some of the most spectacular examples are found in sensory
78 systems: the snout of the star-nosed mole (*Condylura cristata*) has ~25,000
79 mechanosensory organs, several fold more than other mole species (Catania,
80 1995). Male (but not female) moths can have tens of thousands of neurons
81 detecting female pheromones, representing the large majority of sensory neurons
82 in their antennae (Leal, 2013). A higher number of sensory neurons is generally
83 assumed to underlie sensitization to the perceived cues (Kudo et al., 2010; Linz
84 et al., 2013; Meisami, 1989; Peichl, 2005). Surprisingly, however, it remains
85 largely untested if and how such neuronal expansions impact sensory processing
86 and behavior.

87 The drosophilid olfactory system is an excellent model to address these
88 questions (Benton, 2022; Hansson and Stensmyr, 2011). The antenna, the main
89 olfactory organ, houses ~1000 olfactory sensory neurons (OSNs) that, in
90 *Drosophila melanogaster*, have been classified into ~50 types based on their
91 expression of one (or occasionally more) Odorant receptors (Ors) or Ionotropic
92 receptors (Irs) (Benton, 2022; Couto et al., 2005; Grabe et al., 2016). The size of
93 individual OSN populations (ranging from ~10-65 neurons) is stereotyped across
94 individuals, reflecting their genetically hard-wired, developmental programs
95 (Barish and Volkan, 2015; Yan et al., 2020). By contrast, comparisons of
96 homologous OSN types in ecologically-distinct drosophilid species have identified
97 several examples of expansions in OSN populations. Notably, *Drosophila*
98 *sechellia*, an endemic of the Seychelles that specializes on *Morinda citrifolia*
99 “noni” fruit (Auer et al., 2021; Jones, 2005; Stensmyr, 2009), has an
100 approximately three-fold increase in the neuron populations expressing Or22a,

101 Or85b and Ir75b compared to both *D. melanogaster* and a closer relative,
102 *Drosophila simulans* (Auer et al., 2020; Dekker et al., 2006; Ibbá et al., 2010;
103 Prieto-Godino et al., 2017) (**Fig. 1A**). All three of these neuron classes are
104 required for long- and/or short-range odor-guided behaviors (Alvarez-Ocana et
105 al., 2023; Auer et al., 2020) and two of these (Or22a and Ir75b) also display
106 increased sensitivity to noni odors through mutations in the corresponding *D.*
107 *sechellia* receptor genes (Auer et al., 2020; Dekker et al., 2006; Prieto-Godino et
108 al., 2017). Together, these observations have led to a long-held assumption that
109 these OSN population expansions are important for *D. sechellia*, but this has
110 never been tested.

111

112 **Results**

113

114 **Selective large increases in Or22a and Or85b populations in *D. sechellia***

115

116 The increase in Or22a and Or85b OSN numbers in *D. sechellia* reflects the
117 housing of these cells in a common sensory hair, the antennal basiconic 3 (ab3)
118 sensillum (**Fig. 1B, Fig. S1A,B**). To determine how unique this increase is within
119 the antenna, we compared the number of the other ~20 morphologically-diverse,
120 olfactory sensillar classes – which each house distinct, stereotyped combinations
121 of 1-4 OSN types – in *D. sechellia*, *D. melanogaster* and *D. simulans* through
122 RNA FISH of a diagnostic *Or* per sensillum (combined with published data on *Ir*
123 neurons (Prieto-Godino et al., 2017)) (**Fig. 1C**). We observed several differences
124 in sensillar number between these species, including reductions in ab5, ab8 and
125 ai1 in *D. sechellia*, but only ab3, as well as ac3I that house Ir75b neurons,
126 showed a more than two-fold increase (~50 more ab3, 2.6-fold increase; ~15
127 more ac3I, 3.7-fold increase) in *D. sechellia*. The total number of antennal sensilla
128 is, however, similar across species (**Fig. 1C**).

129

130 **OSN population expansion is a complex genetic trait**

131

132 We next investigated the mechanism underlying the ab3 OSN population
133 expansion in *D. sechellia*. The number of ab3 sensilla was not different when
134 these flies were grown in the presence or absence of noni substrate (**Fig. S1C**),
135 arguing against an environmental influence. We first asked whether the ab3
136 increase could be explained by simple transformation of sensillar fate. Previous
137 electrophysiological analyses reported loss of ab2 sensilla in *D. sechellia*, which
138 was interpreted as a potential trade-off for the ab3 expansion (Dekker et al.,
139 2006; Stensmyr et al., 2003). However, we readily detected ab2 sensilla
140 histologically in this species (**Fig. 1C, Fig. S1D**), countering this possibility.
141 Moreover, from an antennal developmental fate map in *D. melanogaster* (Chai et
142 al., 2019), we did not observe any obvious spatial relationship between the
143 sensory organ precursors for sensillar classes that display increases or
144 decreases in *D. sechellia* to support a hypothesis of a simple fate switch,
145 although both expanded populations (ab3 and ac3I) originate from peripheral
146 regions of the map (**Fig. S1E**).

147

148 We therefore reasoned that genetic changes specifically affecting the
149 development of the ab3 lineage might be involved. We first tested for the
150 existence of species-specific divergence in *cis*-regulation at the receptor loci.
Using mutants for both *Or22a(b)* and *Or85b* in *D. simulans* and *D. sechellia*

151 (Auer et al., 2020), we analyzed receptor expression in interspecific hybrids and
152 reciprocal hemizygotes (lacking transcripts from one or the other receptor allele)
153 (**Fig. 1D, Fig. S1F**). In all hybrid allelic combinations (except those lacking both
154 alleles) we observed a similar number of Or22a and Or85b OSNs, arguing
155 against a substantial contribution of *cis*-regulatory evolution at these loci to the
156 expansion of receptor neuronal expression.

157 As little is known about the developmental program of ab3 specification,
158 we used an unbiased, whole-genome, quantitative trait locus (QTL) mapping
159 strategy to characterize the genetic basis of the expansion in *D. sechellia*. For
160 high-throughput quantification of ab3 numbers, we generated fluorescent
161 reporters of Or85b neurons in *D. sechellia* and *D. simulans* (**Fig. S2A,B**).
162 Interspecific F1 hybrids displayed an intermediate number of Or85b neurons to
163 the parental strains (**Fig. 1E**). We phenotyped >600 F2 individuals (backcrossed
164 to either *D. sechellia* or *D. simulans*) (**Fig. 1E**), which were then genotyped using
165 multiplexed shotgun sequencing (Andolfatto et al., 2011). The resulting QTL map
166 (**Fig. 1F**) identified two genomic regions linked to variation in Or85b neuron
167 number located on chromosomes 3 and X; these explain a cell number difference
168 of about ~12 and ~7 neurons, respectively, between *D. sechellia* and *D. simulans*
169 (**Fig. 1G**). No significant epistasis was detected between these genomic regions
170 (**Methods**) and the relatively low effect size (21.0% and 12.3%, respectively) is
171 consistent with a model in which more than two loci contribute to the species
172 difference in Or85b neuron number. Consistent with the QTL map, introgression
173 of fragments of the *D. sechellia* genomic region spanning the chromosome 3
174 peak into a *D. simulans* background led to an increased number of Or85b
175 neurons (**Fig. S2C,D**). However, the phenotypic effect was lost with smaller
176 introgressed regions, indicating that multiple loci influencing Or85b neuron
177 number are located within this QTL region (**Fig. S2D**).

178 In a separate QTL mapping of the genetic basis for the increase in ac3I
179 (Ir75b) neurons in *D. sechellia* (Prieto-Godino et al., 2017) (**Fig. 1C**), we also
180 observed a complex genetic architecture of this interspecific difference, with no
181 evidence for shared loci with the ab3 sensilla expansion (**Fig. S2J,K**). Thus, in
182 contrast to the evolution of sensory specificity of olfactory pathways – where only
183 one or a few amino acid substitutions in a single receptor can have a phenotypic
184 impact (Alvarez-Ocana et al., 2023; Auer et al., 2020; Prieto-Godino et al., 2017),
185 with some evidence for “hotspot” sites in different receptors (Prieto-Godino et al.,
186 2021) – species differences in the number of OSN types have arisen from distinct
187 evolutionary trajectories involving changes at multiple loci.

188 **Or22a is required for *D. sechellia* to track host odor**

189
190
191 We next investigated if and how increased OSN population size impacts odor-
192 tracking behavior. Previously, we showed that both Or22a and Or85b pathways
193 are essential for long-range attraction to noni in a wind tunnel (Auer et al., 2020).
194 To analyze the behavioral responses of individual animals to odors with greater
195 resolution, we developed a tethered fly assay (Badel et al., 2016) with a timed
196 odor-delivery system (**Fig. 2A**). By measuring the beating amplitude of both wings
197 while presenting a lateralized odor stimulus, we could quantify attractive
198 responses to individual odors, as reflected in an animal’s attempt to turn toward
199 the stimulus source, leading to a positive delta wing beat amplitude (ΔWBA) (see
200 **Methods**). We first tested responses of wild-type flies to consecutive short pulses

201 of noni odors, which mimic stimulus dynamics in a plume. As expected, multiple
202 strains of *D. sechellia* displayed attractive responses that persisted through most
203 or all of the series of odor pulses, while *D. melanogaster* strains displayed much
204 more variable degrees of attraction (**Fig. 2B, Fig. S3A**). The persistent attraction
205 in *D. sechellia* was specific to noni odor and could not be observed using apple
206 cider vinegar (**Fig. S3B**).

207 To assess the contribution of distinct olfactory pathways to noni attraction,
208 we tested *D. sechellia* mutants for *Or22a*, *Or85c/b*, *Ir75b* and, as a control,
209 *Or35a*, whose OSN population is also enlarged (as it is paired with *Ir75b* neurons
210 in *ac3l*) but is dispensable for noni attraction (Auer et al., 2020). Loss of *Or22a*
211 abolished attraction of flies towards noni, while *Or85c/b* and *Ir75b* mutants
212 retained some, albeit transient, turning towards this stimulus. Flies lacking *Or35a*
213 behaved comparably to wild-type strains (**Fig. 2C**). These results point to *Or22a*
214 as an important (albeit not the sole) olfactory receptor required for *D. sechellia*
215 to respond behaviorally to noni odor.

216 To better understand the nature of *D. sechellia* plume-tracking in a more
217 natural setting, we used a wind-tunnel assay combined with 3D animal tracking
218 (Straw et al., 2011) to record trajectories of freely-flying wild-type *D. melanogaster*
219 and *D. sechellia*, as they navigated to the source of a noni juice odor plume (**Fig.**
220 **2D, Fig. S4A,B**). Wild-type *D. sechellia* exhibited similar cast and surge dynamics
221 as *D. melanogaster* (van Breugel and Dickinson, 2014) (**Fig. 2D**). However, we
222 observed that *D. sechellia* maintained flight paths closer to the plume centerline
223 (**Fig. 2D-F**), a difference that was particularly evident close (<20 cm) to the plume
224 source (**Fig. 2D-F**). Consistent with the phenotype observed in the tethered-fly
225 assay, *D. sechellia Or22a* mutants lacked strong plume-tracking responses (**Fig.**
226 **2D-F**), while not exhibiting obvious impairment in flight performance (**Fig. S4C**).
227 To extend analysis of these observations we quantified the distribution of flies
228 within a 3 cm radius of the estimated odor plume centerline in the downwind and
229 upwind halves of the wind tunnel (**Fig. 2E,G**). In the downwind half, wild-type *D.*
230 *sechellia* and *D. melanogaster* had comparable course direction distributions
231 (**Fig. 2G**). By contrast, in the upwind half, *D. sechellia* maintained a tighter upwind
232 course distribution suggesting they were more likely to be in an upwind surging
233 state compared to *D. melanogaster* as they approach the odorant source (**Fig.**
234 **2G**). *D. sechellia Or22a* mutants did not appear to be strongly oriented into the
235 wind, notably in the downwind half, further indicating the importance of this
236 olfactory pathway in stereotypical plume-tracking behaviors (**Fig. 2G**).

237
238 ***D. sechellia*'s increase in OSN number is important for persistent odor-**
239 **tracking behavior**

240
241 To investigate the importance of *Or22a* neuron number for odor-tracking behavior
242 we expressed *CsChrimson* in *Or22a* neurons in *D. melanogaster* and *D. sechellia*
243 to enable specific stimulation of this pathway with red light. This optogenetic
244 approach had two advantages: first, it allowed us to calibrate light intensity to
245 ensure equivalent *Or22a* OSN activation between species; second, because only
246 *Or22a* neurons are activated by light, we could eliminate sensory contributions
247 from other olfactory pathways that have overlapping odor tuning profiles to *Or22a*.

248 We first confirmed light-evoked spiking in *Or22a* neurons in *D.*
249 *melanogaster* and *D. sechellia* and determined the light intensity evoking
250 equivalent spike rates (**Fig. 3A**). We then performed lateralized optogenetic

251 activation (Gaudry et al., 2013) of Or22a OSNs in the tethered fly assay,
252 mimicking lateralized odor input by focusing the light beam on one antenna (**Fig.**
253 **3A, Fig. S5A**). Pulsed optogenetic activation of *D. sechellia* Or22a OSNs induced
254 attractive behavior with a similar magnitude and dynamics as pulsed odor stimuli
255 (**Fig. 3B**), demonstrating the sufficiency of this single olfactory pathway for
256 evoking behavior. Notably, the attractive behavior was more persistent over the
257 series of light pulses in *D. sechellia* than in *D. melanogaster* (**Fig. 3A, Fig. S5B-**
258 **D**), consistent with a hypothesis that a higher number of Or22a OSNs supports
259 enduring behavioral attraction to a repeated stimulus.

260 To explicitly test this possibility, we generated genetic tools to reproducibly
261 manipulate the number of active Or22a OSNs in *D. sechellia*, using the SPARC
262 technology developed in *D. melanogaster* (Isaacman-Beck et al., 2020) (**Fig.**
263 **S6A**). Combining a *SPARC2-D-CsChrimson* transgene with *Or22a-Gal4* allowed
264 us to optogenetically stimulate ~50% of these neurons (**Fig. 3C, Fig. S6B**).
265 Although we confirmed light-evoked Or22a neuron spiking in these animals, they
266 did not display attractive behavior towards the light stimulus, in contrast to similar
267 stimulation of all Or22a OSNs (**Fig. 3C, Fig. S6C**). This result implies that the
268 number of active OSNs is critical to induce attraction in *D. sechellia*.

269 Optogenetic activation of Or22a neurons only partially mimics differences
270 between species because it does not offer the opportunity for any possible
271 plasticity in circuit properties that are commensurate with differences in OSN
272 number (as described below). We therefore took a complementary approach,
273 through neuronal silencing, using a *SPARC2-D-Tetanus Toxin (TNT)* transgene.
274 With this tool we could silence on average ~50% of Or22a OSNs (**Fig. 3D**) –
275 likely from mid/late-pupal development (when the *Or22a* promoter is activated
276 (Pan et al., 2017)) – without directly inhibiting other peripheral or central neurons
277 (**Fig. S6D**). Importantly, when tested in our tethered flight assay, these flies
278 showed weaker and more transient attraction towards noni odor, contrasting with
279 the persistent noni attraction of control animals (**Fig. 3D**). Together these results
280 support the hypothesis that the increased Or22a OSN number observed in *D.*
281 *sechellia* is essential for strong and sustained attractive olfactory behavior.

282 283 **OSN population expansions lead to increased pooling on cognate** 284 **projection neurons**

285
286 To better understand how increased OSN number might enhance odor-guided
287 behavior, we first characterized the anatomical properties of the circuitry. The
288 axons of OSNs expressing the same receptor converge onto a common
289 glomerulus within the antennal lobe in the brain (Schlegel et al., 2021) (**Fig. 4A**).
290 Here, they form cholinergic synapses on mostly uniglomerular projection neurons
291 (PNs) – which transmit sensory signals to higher olfactory centers – as well as on
292 broadly-innervating local interneurons (LNs) and a small proportion on other
293 OSNs (Mosca and Luo, 2014; Schlegel et al., 2021). To visualize PNs in *D.*
294 *sechellia*, we generated specific driver transgenes in this species using constructs
295 previously-characterized in *D. melanogaster* (Elkahlah et al., 2020; Tirian and
296 Dickson, 2017): *VT033006-Gal4*, which drives expression in many uniglomerular
297 PN types and *VT033008-Gal4* which has sparser PN expression (**Fig. 4B**). Using
298 these drivers to express photoactivable-GFP in PNs, we performed spatially-
299 limited photoactivation of the DM2 and VM5d glomeruli – which receive input from
300 Or22a and Or85b OSNs, respectively (**Fig. 4A**) – to visualize the partner PNs.

301 We confirmed that DM2 is innervated by 2 PNs in both *D. melanogaster* and *D.*
302 *sechellia* (Auer et al., 2020) and further found that VM5d also has a conserved
303 number of PNs (on average 4) in these species (**Fig. 4C**). Together with data that
304 the Ir75b glomerulus, DL2d, has the same number of PNs in *D. melanogaster*, *D.*
305 *simulans* and *D. sechellia* (Ellis et al., 2023; Prieto-Godino et al., 2017), these
306 observations indicate that *D. sechellia*'s OSN population expansions are not
307 accompanied by increases in PN partners.

308 Next, we expressed a post-synaptic marker, the GFP-tagged D α 7
309 acetylcholine receptor subunit, in PNs (Leiss et al., 2009; Mosca et al., 2017;
310 Mosca and Luo, 2014) in *D. melanogaster* and *D. sechellia* (**Fig. 4D**).
311 Quantification of glomerular volume as visualized with this reporter confirmed
312 previous observations, using OSN markers (Auer et al., 2020; Dekker et al., 2006;
313 Ellis et al., 2023; Ibba et al., 2010; Prieto-Godino et al., 2017), that the DM2 and
314 VM5d glomeruli, but not a control glomerulus (DM6), are specifically increased in
315 *D. sechellia* compared to *D. melanogaster* (**Fig. 4E**). Given the constancy in PN
316 number (**Fig. 4C**), this observation implied that PN dendrites must exhibit
317 anatomical differences to occupy a larger volume. We examined this possibility
318 through visualization of single VM5d PNs by dye-labelling (in the course of
319 electrophysiology experiments described below). Reconstruction of dendrite
320 morphologies revealed that *D. sechellia* VM5d PNs have increased dendritic
321 surface area and volume compared to the homologous neurons in *D.*
322 *melanogaster* (**Fig. 4F**).

323 Finally, we quantified post-synaptic puncta of D α 7:GFP to estimate the
324 number of excitatory OSN-PN connections in these glomeruli. Both DM2 and
325 VM5d, but not DM6, displayed more puncta in *D. sechellia* than in *D.*
326 *melanogaster* (**Fig. 4G**). Although quantifications of fluorescent puncta are likely
327 to substantially underestimate the number of synapses detectable by electron
328 microscopy (Mosca and Luo, 2014; Schlegel et al., 2021), this reporter should still
329 reflect the relative difference between species. Together these data suggest that
330 an increase in OSN numbers leads to larger glomerular volumes, increased
331 dendritic arborization in partner PNs and overall more synaptic connections
332 between OSNs and PNs.

333

334 **OSN number increases do not lead to sensitization of PN responses**

335

336 To investigate the physiological significance of these OSN-PN circuit changes, we
337 generated genetic reagents to visualize and thereby perform targeted
338 electrophysiological recordings from specific PNs. We focused on VM5d PNs due
339 to the availability of an enhancer-Gal4 transgene for sparse genetic labelling of
340 this cell type (Li et al., 2020). Moreover, the partner Or85b OSNs' sensitivities to
341 the best-known agonist, 2-heptanone, are indistinguishable between species
342 (Auer et al., 2020), enabling specific assessment of the impact of OSN population
343 expansion on PN responses. Through whole-cell patch clamp recordings from
344 VM5d PNs in *D. melanogaster* and *D. sechellia* (**Fig. 5A**), we first observed that
345 the input resistance of these cells was ~2-fold lower in *D. sechellia* (**Fig. 5B**),
346 consistent with their larger dendritic surface area and volume (**Fig. 4F**). The
347 resting membrane potential (**Fig. 5C**) and spontaneous activity (**Fig. 5D**) of these
348 PNs were, however, unchanged between species. Surprisingly, VM5d PNs
349 displayed no obvious increase in odor sensitivity in *D. sechellia* (**Fig. 5E, Fig.**
350 **S7A**); if anything, the peak spiking rate (within the first 50 ms after PN response

351 onset) tended to be higher in *D. melanogaster*. However, we observed that the
352 PN firing during the odor stimulus displayed a starker decay in *D. melanogaster*
353 than *D. sechellia* (**Fig. 5F, Fig. S7B**). These data support a model in which
354 increased synaptic input by more OSNs in *D. sechellia* is compensated by
355 decreased PN input resistance precluding the sensitization of responses in this
356 cell type. Instead, OSN increases might impact the temporal dynamics of PN
357 responses (explored further below).

358 To substantiate and extend these observations, we expressed GCaMP6f
359 broadly in OSNs or PNs and measured odor-evoked responses in specific
360 glomeruli using two-photon calcium imaging. When measuring calcium responses
361 to a short pulse of 2-heptanone in Or85b OSN axon termini in the VM5d
362 glomerulus, we observed, as expected (Auer et al., 2020), no sensitivity
363 differences (**Fig. 5G, Fig. S8A**). VM5d PNs also displayed no obvious increase in
364 odor sensitivity in *D. sechellia* (**Fig. 5G, Fig. S8B**), consistent with our patch
365 clamp recordings (**Fig. 5E**). Next, we investigated Or22a OSNs and DM2 PNs
366 after stimulation with the noni odor methyl hexanoate (Dekker et al., 2006). In this
367 olfactory pathway, *D. sechellia* OSNs displayed responses at odor concentrations
368 approximately two orders of magnitude lower than in *D. melanogaster* (**Fig. 5H,**
369 **Fig. S8C**), concordant with previous electrophysiological analyses (Auer et al.,
370 2020; Dekker et al., 2006; Stensmyr et al., 2003). *D. sechellia* DM2 PNs
371 displayed a similar degree of heightened sensitivity compared to those in *D.*
372 *melanogaster*, supporting that an increased Or22a OSN number does not lead to
373 further sensitization of these PNs (**Fig. 5H, Fig. S8D**). To test the sufficiency of
374 differences in receptor properties (Auer et al., 2020) to explain PN activity
375 differences, we expressed *D. melanogaster* or *D. sechellia* Or22a in *D.*
376 *melanogaster* Or22a neurons lacking the endogenous receptors. This
377 manipulation conferred a species-specific odor response profile to these OSNs
378 (Auer et al., 2020). Measurement of responses to methyl hexanoate in DM2 PNs
379 revealed higher sensitivity in animals expressing *D. sechellia* Or22a compared to
380 those expressing *D. melanogaster* Or22a (**Fig. S8E**); notably, this difference was
381 similar in magnitude to the endogenous sensitivity differences of *D. sechellia* and
382 *D. melanogaster* DM2 PNs. Together, the analyses of Or85b and Or22a
383 pathways indicate that a larger OSN population does not contribute to enhanced
384 PN sensitization.

385 386 **OSN number increases do not lead to increased reliability of PN responses**

387
388 Pooling of inputs on interneurons has also been suggested to reduce the noise in
389 central sensory representations, since spontaneous activity of each OSN is
390 uncorrelated and becomes averaged out as OSN activities are summated at PNs
391 (Bhandawat et al., 2007; Jeanne and Wilson, 2015; Serences, 2011). This
392 phenomenon should reduce the variability of PN response magnitude across
393 multiple odor presentations. We therefore examined whether increased OSN
394 number plays a role in reducing trial-to-trial variability in PN responses by
395 comparing odor responses, and their variation, in VM5d PNs to eight trials of 2-
396 heptanone stimulation. These experiments did not reveal any differences in PN
397 response reliability between *D. melanogaster* and *D. sechellia* (**Fig. S9**).
398 Consistent with this calcium imaging analyses, the lack of a significant difference
399 in VM5d PN spontaneous spiking frequency between species (**Fig. 5D**) also

400 argues that increased sensory pooling in *D. sechellia* does not substantially
401 reduce noise in this circuitry.

402

403

404

405 **Pathways with increased OSN number display reduced decay magnitude of**
406 **PN responses**

407

408 Most natural odors exist as turbulent plumes, which stimulate OSNs with
409 complex, pulsatile temporal dynamics (van Breugel and Dickinson, 2014). To test
410 if odor temporal dynamics in these olfactory pathways are influenced by OSN
411 number, we repeated the calcium imaging experiments using ten consecutive,
412 short pulses of odor. Or85b OSNs displayed a plateaued response to pulses of 2-
413 heptanone in both *D. melanogaster* and *D. sechellia*, albeit with a slight decay
414 over time in the latter species (**Fig. 5I**). *D. melanogaster* VM5d PNs showed
415 decreasing responses following repeated exposure to short pulses, presumably
416 reflecting adaptation, as observed in multiple PN types (Kazama and Wilson,
417 2008). By contrast, VM5d PNs in *D. sechellia* displayed responses of similar
418 magnitude throughout the series of odor pulses (**Fig. 5J**). This species difference
419 in PN responses was also seen with long-lasting odor stimulation (**Fig. S10**) and
420 is consistent with a smaller difference between spiking frequencies at the start
421 and end of odor stimulation in *D. sechellia* VM5d PNs measured by
422 electrophysiological recordings (**Fig. 5F and S7B**). Imaging the responses of
423 Or22a OSN partner PNs in DM2 to pulsed odor stimuli (using concentrations of
424 methyl hexanoate that evoked similar activity levels between the species (**Fig.**
425 **5H**)) revealed a similar result: *D. melanogaster* DM2 PN responses decreased
426 over time while *D. sechellia* DM2 PNs responses were unchanged in magnitude
427 (**Fig. 5K**). However, for two olfactory pathways where the numbers of cognate
428 OSNs are not increased in *D. sechellia* (Or59b (DM4) and Or92a (VA2) (**Fig.**
429 **1C**)), the PNs in both species displayed decreasing responses over the course of
430 stimulations (**Fig. 5L,M, Fig. S11**). Together, our data indicate that OSN number
431 increases in *D. sechellia*'s noni-sensing pathways might result, directly or
432 indirectly, in reduced decay magnitude of PN responses to dynamic or long-
433 lasting odor stimuli.

434

435 **Species-specific PN response properties are due, at least in part, to**
436 **differences in lateral inhibition**

437

438 More sustained PN responses in *D. sechellia* could be due to species differences
439 in several aspects of glomerular processing, involving OSNs, PNs and/or LNs.
440 We examined this phenomenon through calcium imaging in VM5d PNs before
441 and after pharmacological inhibition of different synaptic components. Blockage of
442 inhibitory neurotransmission – which is principally mediated by LNs acting broadly
443 across glomeruli (Liu and Wilson, 2013; Olsen et al., 2010; Wilson and Laurent,
444 2005) – decreased adaptation in *D. melanogaster* VM5d PNs, as expected. This
445 effect was predominantly due to inhibition of GABA_B rather than GABA_A/GluCl
446 receptors (**Fig. S12A,B**). By contrast, inhibitory neurotransmitter receptor
447 blockage did not lead to changes in temporal dynamics of responses in *D.*
448 *sechellia* (**Fig. 6A and Fig. S12A,B**). These observations suggest that
449 differences in the strength of inhibition between species contribute to differences

450 in PN decay magnitude (see Discussion). We note that *D. sechellia* PNs
451 displayed apparent decreases in odor response magnitude (as measured by
452 $\Delta F/F$) upon pharmacological treatment (**Fig. 6A**), but this effect is most likely due
453 to elevated baseline activity (F_0) in this species (**Fig. S12C**).

454 We next pharmacologically impaired cholinergic neurotransmission to
455 diminish excitatory connections of OSNs, which include OSN-PN and likely also
456 OSN-LN synapses (Huang et al., 2010; Kazama and Wilson, 2008; Schlegel et
457 al., 2021; Wilson, 2013). As expected, strong blockage essentially abolished
458 odor-evoked PN responses (data not shown). More informatively, weak blockage
459 led to enhanced decay in the VM5d PN responses of *D. sechellia* (**Fig. 6B**), as
460 seen in untreated *D. melanogaster* (**Fig. 6B**). These observations suggest that
461 excitatory neurotransmission from OSNs to PN and/or LNs also contributes to the
462 temporal dynamics of PN responses. Consistent with this possibility, halving the
463 number of OSN inputs in *D. sechellia* through removal of one antenna (OSN
464 axons project to antennal lobes in both brain hemispheres (Schlegel et al., 2021))
465 enhanced the decay of this species' VM5d PN responses (**Fig. 6C**). These data
466 support the hypothesis that OSN number increase in *D. sechellia* modulates PN
467 response dynamics.

468

469 Discussion

470

471 Amongst the many ways in which animal brains have diverged during evolution,
472 species-specific increases in the number of a particular neuron type are one of
473 the most common. The genetic basis and physiological and behavioral
474 consequences of such apparently simple changes have, however, remained
475 largely unexamined. Here we have exploited an ecologically and phylogenetically
476 well-defined model clade of drosophilids to study this phenomenon. We provide
477 evidence that expansion of host fruit-detecting OSN populations in *D. sechellia* is
478 a complex trait, involving contributions of multiple loci. Surprisingly, a larger
479 number of OSNs does not result in sensitization of partner PNs nor in increased
480 reliability of their responses. Rather we observed more sustained responses of
481 PNs upon repetitive or long-lasting odor stimulation. While OSN number alone
482 can influence the strength and persistence of odor-tracking behavior, this
483 species-specific cellular trait is likely to synergize with increases in peripheral
484 sensory sensitivity conferred by changes in olfactory receptor tuning properties
485 (Auer et al., 2020; Dekker et al., 2006; Prieto-Godino et al., 2017) to enable long-
486 distance localization of the host fruit of this species (**Fig. 6D**).

487 One important open question is how OSN population increases affect
488 circuit properties and behavior. For one experimentally-accessible glomerulus,
489 VM5d, we observed that PNs (which are unchanged in number between species)
490 have a larger surface area and form more synapses with OSNs but show lower
491 dendritic input resistance in *D. sechellia*. This anatomical and physiological
492 compensation results in the voltage responses of PNs being very similar between
493 species despite the increased OSN input in *D. sechellia*. Such compensation
494 might reflect in-built plasticity in glomerular microcircuitry. Indeed, *D.*
495 *melanogaster* shows intra-species difference in OSN number across glomeruli
496 (Grabe et al., 2016) and the number of OSNs correlates with synapse number
497 (**Fig. S13A** (Schlegel et al., 2021)). Moreover, a previous study in *D.*
498 *melanogaster* characterized the consequence of (random) differences in PN
499 numbers in a glomerulus (DM6): in glomeruli with fewer PNs (i.e. greater sensory

500 convergence per neuron), individual PNs had larger dendrites, formed more
501 synapses with OSNs, and exhibited lower input resistance (Tobin et al., 2017),
502 analogous to our observations in *D. sechellia* VM5d.

503 Species-specific physiological responses to prolonged or repetitive odor
504 stimuli likely involves multiple neuron classes. In *D. melanogaster*, adaptation of
505 PNs to long odor stimuli occurs through lateral inhibition by GABAergic LNs
506 (Nagel et al., 2015; Wilson and Laurent, 2005), as we confirmed here. However,
507 such inhibition appears to be weaker in *D. sechellia* in pathways with more OSNs.
508 Given the conserved total number of antennal OSNs between species, more
509 OSNs in one pathway could lead to stronger inhibitory neurotransmission from
510 the correspondingly larger glomerulus to other unchanged or smaller glomeruli.
511 Critically, this could result in net weaker lateral inhibition from these glomeruli
512 onto the expanded glomerulus, as seen in *D. sechellia*. We cannot exclude that
513 LNs display species-specific innervations or connectivity, but testing this idea will
514 require genetic drivers to visualize and manipulate subsets of this highly diverse
515 neuron type (Chou et al., 2010). Finally, we note that it is also possible that
516 differences exist in the intrinsic physiology of PNs due to, for example, differential
517 expression of ion channels between species. Such differences – potentially
518 unrelated to changes in OSN number – might be revealed by mining comparative
519 transcriptomic datasets for these drosophilids (Lee and Benton, 2023).

520 Regardless of the precise mechanism, could more sustained PN
521 responses convert to behavioral persistence? The main post-synaptic partners of
522 PNs are lateral horn neurons and Kenyon cells, of which the latter (at least) have
523 a high input threshold (Turner et al., 2008) for sparse coding. Assuming the
524 threshold of these neurons is commensurate with maximum PN firing rate (which
525 is higher in *D. melanogaster*), the relaxed decay in PN activity in *D. sechellia*
526 might elongate downstream responses to persistent odors, which could drive
527 valence-specific behaviors (Aso et al., 2014). Sensory habituation is
528 advantageous for the brain to avoid information overload by attenuating constant
529 or repetitive inputs and is a general feature across sensory modalities (O'Mahony,
530 1986). However, this phenomenon might be disadvantageous when navigating
531 through sensory cues for a long period of time, for example, during olfactory
532 plume-tracking. The reduced adaptation selectively in PNs in the expanded
533 sensory pathways in *D. sechellia* that detect pertinent host odors provides an
534 elegant resolution to this conflict in sensory processing, leaving conserved
535 molecular effectors mediating synaptic neurotransmission and adaptation in other
536 olfactory pathways intact.

537 Beyond *D. sechellia*, selective increases in ab3 neuron numbers have
538 been reported in at least two other drosophilid species, which are likely to
539 represent independent evolutionary events (Keesey et al., 2022; Linz et al., 2013)
540 (**Fig. S13B**). Furthermore, Or22a neurons display diversity in their odor specificity
541 across drosophilids (de Bruyne et al., 2010; Keesey et al., 2022). These
542 observations suggest that this sensory pathway is an evolutionary “hotspot”
543 where changes in receptor tuning and OSN population size collectively impact
544 sensory processing, perhaps reflecting the potent behavioral influence of this
545 pathway, as we have found in *D. sechellia*. More generally, given our
546 demonstration of the important effect of OSN population size on host odor
547 processing in *D. sechellia*, examination of how cell number increases modify
548 circuit properties in other sensory systems, brain regions and species seems
549 warranted.

550

551 **Acknowledgements**

552

553 We thank Hokto Kazama, Johannes Larsch, Silke Sachse and members of the
554 Benton laboratory for discussions and/or comments on the manuscript. We are
555 grateful to Yoshi Aso, John Carlson, Sophie Caron, Tom Clandinin, Heather
556 Dionne, Lukas Neukomm, Gerald Rubin, Stephan Sigrist, the Bloomington
557 *Drosophila* Stock Center (NIH P40OD018537) and the Developmental Studies
558 Hybridoma Bank (NICHD of the NIH, University of Iowa) for reagents. We also
559 thank Jesse Isaacman-Beck for construct design, Anabela Rebelo Pimentel for
560 her assistance with embryo alignments for microinjections, and the Lausanne
561 Genomic Technologies Facility for sequencing. S.T. was supported by a Marie
562 Skłodowska-Curie Actions Individual Fellowship (836783), an EMBO Long-Term
563 Fellowship (ALTF 454-2019) and a Japanese Society for the Promotion of
564 Science (JSPS) Overseas Research Fellowship (202360258). Research in
565 J.R.A.'s lab was supported by the Swiss National Science Foundation
566 (PP00P3_176956 and 310030_201188). C.F.R.W. was support by a National
567 Institutes of Health grant (R01EY022638) to Tom Clandinin. F.v.B.'s laboratory
568 was supported by the Air Force Office of Scientific Research (FA9550-21-0122).
569 G.S. and J.M.J. were supported by NIH grants R01 DC018570 and R01
570 NS116584, the Richard and Susan Smith Family Award for Excellence in
571 Biomedical Research, the Klingenstein-Simons Fellowship Award in
572 Neuroscience, and an innovative research award from the Kavli Institute for
573 Neuroscience at Yale University to J.M.J. T.O.A. and his laboratory were
574 supported by a Human Frontier Science Program Long-Term Fellowship
575 (LT000461/2015-L), a Swiss National Science Foundation Ambizione Grant
576 (PZ00P3 185743) and the Fondation Pierre Mercier pour la science. R.B.'s
577 laboratory was supported by the University of Lausanne, the Swiss National
578 Science Foundation (310030B-185377) and ERC Consolidator (615094) and
579 Advanced (833548) Grants.

580

581 **Author Contributions**

582

583 S.T., T.O.A. and R.B. conceived the project. All authors contributed to
584 experimental design, analysis and interpretation of results. Specific experimental
585 contributions were as follows: S.T. performed all calcium imaging,
586 photoactivation, tethered fly behavioral experiments and cloning of the
587 *VT033006-LexA* construct. T.O.A. performed molecular biology experiments,
588 generated transgenic lines, performed histology, Or85b QTL analysis, cell
589 number quantifications and electrophysiology. G.S. performed PN
590 electrophysiology, dye-filling and anatomical analysis, with guidance from J.M.J.
591 L.A. performed molecular biology experiments, histology and quantifications of
592 post-synaptic puncta. S.D.S. performed the wind tunnel behavioral experiments,
593 with guidance from F.v.B. J.R.A. performed the Ir75b QTL analysis and
594 contributed to the Or85b QTL analysis. L.L.P.-G. performed the Ir75b QTL
595 analysis. D.L.S. contributed to the QTL analyses and generated the *UAS-*
596 *CsChrimson* construct. S.C. contributed to the Ir75b QTL analysis. R.A.O.
597 performed histology in the *D. melanogaster* subgroup. C.F.R.W. generated the
598 parent *SPARC2-TNT* construct. S.T., T.O.A. and R.B. wrote the paper with input
599 from all other authors. All authors approved the final version of the manuscript.

600

601 **Declaration of interests**

602

603 The authors declare no competing interests.

604

605

606 **Methods**

607

608 **Data reporting**

609 Preliminary experiments were used to assess variance and determine adequate
610 sample sizes in advance of acquisition of the reported data. For
611 electrophysiological recordings, data were collected from multiple flies on several
612 days in randomized order. Within datasets, the same odor dilutions were used for
613 acquisition of the data. The experimenter was blinded to the genotype for
614 quantification of OSN numbers, and SPARC2-CsChrimson and SPARC2-TNT
615 tethered fly assays, but not for other behavioral or physiological experiments.

616

617 ***Drosophila* strains**

618 *Drosophila* stocks were maintained on standard wheat flour/yeast/fruit juice
619 medium or, for those used in PN electrophysiology experiments, semi-defined
620 culture medium (Backhaus et al., 1984) under a 12 h light:12 h dark cycle at
621 25°C. For all *D. sechellia* strains, a few g of Formula 4-24® Instant *Drosophila*
622 Medium, Blue (Carolina Biological Supply Company) soaked in noni juice (Raab
623 Vitalfood or Tahiti Trader) were added on top of the standard food. Wild-type,
624 mutant and transgenic *Drosophila* lines used in this study are listed in
625 **Supplemental Table 2.**

626 To generate *lozenge* (*lz*) trans-heterozygous *D. simulans*/*D. sechellia*
627 hybrid flies, we group-aged 25-35 virgin males of *D. simulans* (*Dsim03 Or85b^{GFP}*
628 or *Dsim03 lz^{RFP};Or85b^{GFP}*) for 6-7 days before combining them with 20-30 virgin
629 females of *D. sechellia* (*Dsec07 lz^{RFP};Or85b^{GFP}* or *Dsec07 Or85b^{GFP}*). We
630 lowered the fly food cap to restrict space and force interactions between the
631 animals (which otherwise had a very low tendency to mate). Tubes were
632 maintained at 22°C with strong light exposure and flipped every 3-4 days into a
633 new tube. Progeny were collected and phenotyped 7-10 days post-eclosion.

634

635 **Constructs for CRISPR/Cas9-mediated genome engineering and** 636 **transgenesis**

637 *D. simulans Or85b*: for expression of a single sgRNA targeting the *D. simulans*
638 *Or85b* locus, an oligonucleotide pair (**Supplemental Table 3**) was annealed and
639 cloned into *BbsI*-digested *pCFD3-dU6-3gRNA* (Addgene #49410) as described
640 (Port et al., 2014). To generate a donor vector for homologous recombination,
641 homology arms (1-1.6 kb) were amplified from *D. simulans* (*Drosophila* Species
642 Stock Center [DSSC] 14021-0251.195) genomic DNA and inserted into *pHD-*
643 *Stinger-attP* (Auer et al., 2020) via restriction cloning. Both constructs were co-
644 injected with a source of Cas9 (as described below) into *D. simulans* DSSC
645 14021-0251.003 and DSSC 14021-0251.004.

646 *D. simulans* and *D. sechellia lz*: to express multiple sgRNAs targeting the
647 *lz* loci from the same vector backbone, oligonucleotide pairs (**Supplemental**
648 **Table 4**) were used for PCR and inserted into *pCFD5* (Addgene #73914) via
649 Gibson Assembly, as described (Port and Bullock, 2016). To generate donor
650 vector for homologous recombination, homology arms (1-1.6 kb) were amplified
651 from *D. sechellia* (DSSC 14021-0248.07) or *D. simulans* (DSSC 14021-0251.195)
652 genomic DNA and inserted into *pHD-DsRed-attP* (Gratz et al., 2014) via Gibson
653 Assembly. Species-specific constructs were co-injected with a source of Cas9 (as
654 described below) into *D. simulans* DSSC 14021-0251.004 or *D. sechellia nos-*
655 *Cas9* (Auer et al., 2020).

656 *D. sechellia* UAS-SPARC2-D-CsChrimson: we digested a SPARC2-
657 backbone vector (Addgene #133562) with *Sall* and inserted a *CsChrimson-Venus*
658 cassette after PCR amplification from *pBac(UAS-ChR2*
659 *CsChrimson,3xP3::dsRed)* via Gibson Assembly. The resulting SPARC2-D-
660 *CsChrimson* cassette was amplified via PCR and inserted via restriction cloning
661 into *pHD-3xP3-DsRed DattP-D. sechellia attP40* (this targeting vector for
662 homologous recombination at the *D. sechellia attP40* equivalent site will be
663 described in more detail elsewhere).

664 *D. sechellia* UAS-SPARC2-D-TNT-HA-GeCO: we first generated a *pHD-*
665 *3xP3-DsRed_DattP-UAS-TNT-GeCO* vector by amplifying a *TNT-GeCO* cassette
666 from *pHD-37.1_AtTP5_LexAop_90_10_TNT-HA_p2A_jRGeCO1a* together with a
667 UAS cassette and insertion into *pHD-3xP3-DsRed DattP* via Gibson Assembly.
668 Subsequently, we transferred the *UAS-TNT-HA-GeCO* cassette into *pHD-3xP3-*
669 *DsRed DattP-D. sechellia attP40* before assembling *pHD-3xP3-DsRed DattP-D.*
670 *sechellia attP40 SPARC2-D-TNT-HA-GeCO* via Gibson Assembly (the GeCO
671 calcium indicator was not used in the current study). Both SPARC-D transgenic
672 lines in *D. sechellia* were generated via CRISPR/Cas9-mediated homologous
673 recombination at the *attP40*-equivalent site in *D. sechellia*. To test the
674 functionality of the *UAS-TNT-HA-GeCO* cassette, we also generated *UAS-TNT-*
675 *HA-GeCO* transgenic lines via homologous recombination at the *attP40* locus in
676 *D. melanogaster* and *D. sechellia*. However, in both species successful
677 transformants did not survive pupariation, which was potentially due to low-level,
678 Gal4-independent expression of the TNT effector.

679 *D. melanogaster* VT033006-LexA: to generate a *VT033006-LexA*
680 construct, *pLexA-SV40-attB* was digested with *NotI*. A *VT033006* enhancer
681 fragment was PCR-amplified from *pVT033006-Gal4-attB* (Tirian and Dickson,
682 2017). The insert and the linearized vector were joined by Gibson assembly. The
683 vector was integrated into *D. melanogaster attP2* by BestGene Inc.

684 *D. sechellia* VT033006-Gal4, VT033008-Gal4 and VM5d-Gal4: constructs
685 carrying the *D. melanogaster* enhancer sequences (Tirian and Dickson, 2017)
686 were integrated into *Dsec-white* (*attP* landing site on the X chromosome (Auer et
687 al., 2020)) or *Dsec-attP40* (see next section). The *Dsec-nSyb-ΦC31* line was
688 generated by integration of *nSyb-ΦC31* (Addgene #133868) into *Dsec-attP26*
689 (see next section).

690 *D. sechellia* UAS-myrGFP: *pUAS-myrGFP*, *QUAS-mtdTomato(3xHA)*
691 (Talay et al., 2017) was integrated into *Dsec-attP40*. *D. sechellia* UAS-
692 *Dα7:GFP*: flies were generated by P-element-mediated transgenesis of *p(UAS-*
693 *Dα7:GFP)* (Leiss et al., 2009) into *D. sechellia* DSSC 14021-0248.30 by
694 WellGenetics.

695 *D. sechellia* *pBac(UAS-CsChrimson-Venus)*: we first amplified a *UAS-*
696 *CsChrimson-Venus* cassette from *pUAS-ChR2 CsChrimson* (Klapoetke et al.,
697 2014) and a *pBac* backbone (Horn and Wimmer, 2000) and combined both via
698 Gibson assembly resulting in *pBac(UAS-CsChrimson-Venus)*. Subsequently, we
699 digested *pBac(UAS-CsChrimson-Venus)* with *Ascl*, amplified a *3xP3-DsRed*
700 cassette (derived from gene synthesis, Genetivision) via PCR and combined both
701 via Gibson Assembly resulting in *pBac(UAS-CsChrimson-Venus,3xP3-DsRed)*.
702 Primer sequences for intermediate cloning steps are listed in **Supplemental**
703 **Table 3**. PiggyBac-mediated transgenesis of *pBac(UAS-CsChrimson-*
704 *Venus,3xP3-DsRed)* into *D. sechellia* DSSC 14021-0248.07 was performed in-
705 house (see below) and the insertion site mapped to the third chromosome using

706 TagMap (Stern, 2017). Beyond its use for optogenetic experiments, we took
707 advantage of the visible 3xP3-DsRed marker to use the same line for
708 introgression mapping (**Figure S2C,D**).

709 All plasmids were verified via Sanger sequencing before injection. Full
710 details and oligonucleotide sequences are available from the corresponding
711 authors upon request.

712

713 ***Drosophila* transgenesis**

714 Except for specific constructs described above, mutagenesis/transgenesis of *D.*
715 *sechellia*, *D. simulans* and *D. melanogaster* was performed in-house following
716 standard protocols (Auer et al., 2020) . For *piggyBac* and P-element
717 transgenesis, we co-injected a *piggyBac* or P-element vector (300 ng μl^{-1}) and
718 *piggyBac* (Arnoult et al., 2013) or P-element helper plasmid (Stern et al., 2017)
719 (300 ng μl^{-1}). For CRISPR/Cas9-mediated homologous recombination, we
720 injected a mix of an sgRNA-encoding construct (150 ng μl^{-1}) and donor vector
721 (500 ng μl^{-1}) into *D. sechellia* nos-Cas9 (Auer et al., 2020) or co-injected with
722 *pHsp70-Cas9* (400 ng μl^{-1}) (Addgene #45945; for *D. simulans* transgenesis)
723 (Gratz et al., 2013). Site-directed integration into *attP* sites was achieved by co-
724 injection of an *attB*-containing vector (400 ng μl^{-1}) and *pBS130* (encoding ΦC31
725 integrase under control of a heat shock promoter (Addgene #26290) (Gohl et al.,
726 2011)). The *Dsec-attP26* site (on chromosome 4) was generated via *piggyBac*-
727 mediated random integration and *Dsec-attP40* via CRISPR-mediated
728 homologous recombination and both will be described in more detail elsewhere.
729 All concentrations are given as final values in the injection mix.

730

731 **Histology**

732 Fluorescent RNA *in situ* hybridization (using digoxigenin- or fluorescein-labelled
733 RNA probes) and immunofluorescence on whole-mount antennae were
734 performed essentially as described (Saina and Benton, 2013; Silbering et al.,
735 2011). Probes were generated using *D. sechellia* genomic DNA (*Or47a*, *Or88a*)
736 and primers listed in **Supplemental Table 3**. Other published probes were either
737 targeting *D. sechellia* (*Or42b*, *Or22a*, *Or85b*, *Or13a*, *Or98a*, *Or35a* (Auer et al.,
738 2020)), *D. simulans* (*Or67a* (Auer et al., 2022)) or *D. melanogaster* transcripts
739 (*Or56a*, *Or59b*, *Or9a*, *Or69aA* (Vosshall et al., 2000); *Or19a* (Couto et al., 2005);
740 *Or83c*, *Or67d* (Chai et al., 2019)); all probes were used at a concentration of
741 1:50. Immunofluorescence on adult brains – with the exception of the
742 visualization of dye-filled PN (described below) – was performed as described
743 (Sanchez-Alcaniz et al., 2017).

744 The following antibodies were used: guinea pig α -Ir75b 1:500
745 (RRID:AB_2631093 (Prieto-Godino et al., 2017)), mouse monoclonal antibody
746 nc82 1:10 (Developmental Studies Hybridoma Bank), rabbit α -GFP 1:500
747 (Invitrogen), and rat α -HA 1:500 (Roche). Alexa488-, Cy3- and Cy5-conjugated
748 goat α -guinea pig, goat α -mouse, goat α -rabbit and goat α -rat IgG secondary
749 antibodies (Molecular Probes; Jackson Immunoresearch) were used at 1:500.

750

751 **Image acquisition and processing**

752 Except for dye-filled PN imaging and analysis (described below), confocal images
753 of antennae and brains were acquired on an inverted confocal microscope (Zeiss
754 LSM 710) with an oil immersion 40 \times objective (Plan Neofluar 40 \times Oil immersion
755 DIC objective; 1.3 NA). For quantification of synapse numbers, images were

756 taken using a 63× objective (Plan-Apochromat 63× Oil immersion DIC M27; 1.4
757 NA) with a zoom of 3×, centering the image on the glomerulus of interest. Images
758 were processed in Fiji (Schindelin et al., 2012). *D. sechellia* brains were imaged
759 and registered to a *D. sechellia* reference brain (Auer et al., 2020) using the Fiji
760 CMTK plugin (<https://github.com/jefferis/fiji-cmtk-gui>).

761 Cell number quantification: the number of OSNs expressing a specific *Or*
762 was quantified using Imaris (Bitplane) or the Fiji Cell Counter tool. For GFP-
763 expressing *Or85b* OSNs for the QTL analysis, we imaged GFP and, in the 568
764 nm channel, cuticular autofluorescence. After subtraction of the cuticular
765 fluorescence signal from the GFP signal using the Subtraction tool in Fiji, we
766 quantified the number of GFP-positive nuclei using the Surface Detection tool in
767 Imaris. For *Ir75b* neurons, we found that α -*Ir75b* immunofluorescence resulted in
768 labelled cells having a range of intensities. To ensure that the cell quantifications
769 were reproducible, counting was performed manually by three experimenters.
770 Images resulting in disagreements were re-checked and either resolved or
771 removed from the analyses.

772 Glomerular and synapse quantification: glomerular volumes were
773 calculated following segmentation with the Segmentation Editor plugin of Fiji
774 using the 3D Manager plugin. The number of post-synaptic sites per glomerulus
775 was quantified in Imaris as described (Mosca and Luo, 2014), setting punctum
776 size to 0.45 μm^3 for all images.

777

778 **Quantitative trait locus mapping**

779 *Or85b* phenotyping: flies expressing nuclear-localized GFP in *Or85b* neurons
780 were placed individually into 96-well plates whose bottom was replaced by a
781 metal mesh. Antennae were removed via shock-freezing in liquid nitrogen and
782 collected in 4% paraformaldehyde-3% Triton-PBS as described (Saina and
783 Benton, 2013). After 3 h of fixation, antennae were washed twice in 3% Triton-
784 PBS and twice in 0.1% Triton-PBS and mounted in Vectashield (Vectorlabs) on
785 30-well PTFE printed slides (Electron Microscopy Sciences) before imaging on a
786 Zeiss LSM710 confocal microscope. The fly bodies were transferred (by
787 inversion) into separate 96-well plates and frozen at -20°C. Genomic DNA of
788 individual flies was extracted using the ZR-96 Quick-gDNA MiniPrep kit (Zymo
789 Research).

790 *Ir75b* phenotyping: flies were processed as described above. For
791 antennae, after washing in 0.1% Triton-PBS, *Ir75b* immunofluorescence was
792 performed. Antennae were mounted in Vectashield (Vectorlabs) on 30-well PTFE
793 printed slides (Electron Microscopy Sciences) before imaging on a Zeiss LSM710
794 confocal microscope.

795 *Sequencing and genotyping*: genomic DNA of individual flies was
796 tagged with in-house produced Tn5 as described (Picelli et al., 2014). In brief,
797 Tn5 was charged with adaptors and mixed at a concentration of 5 ng μl^{-1} with 1 μl
798 of genomic DNA. After tagmentation, Tn5 was de-activated by addition of 0.2%
799 sodium dodecyl-sulphate and sample specific sequencing adaptors were added
800 by PCR amplification. The resulting PCR amplicons were cleaned-up with
801 AMPure XP bead-based reagents (Beckman Coulter Life Science), DNA
802 concentration and fragment distribution quantified on a fragment analyzer
803 (Agilent) and single-end sequenced on an Illumina HiSeq sequencer.

804 *Data analysis*: to align sequencing reads, the parental genomes dsim r2.02
805 and dsec r1.3 were used as reference. Introgressed genomic regions were

806 inferred using MSG software (<http://www.github.com/JaneliaSciComp/msg>).
807 Output of MSG was thinned using the “pull_thin” utility
808 (http://www.github.com/dstern/pull_thin) and read into R (v4.4.1) using the
809 “read_cross_msg” utility (http://www.github.com/dstern/read_cross_msg). QTL
810 mapping was carried out with the qtl package (v1.5) using the Haley-Knott
811 method and significance was determined using 1000 permutation tests (n.perm =
812 1000). For the Or85b mapping experiment, tests for interactions between the QTL
813 on chromosomes 3 and X were performed using the “fitqtl” function.

814

815 **Two-photon calcium imaging**

816 *Animal preparation:* flies of the appropriate genotype (described in the respective
817 figure legends) were collected (females and males co-housed) and reared in
818 standard culture medium (see above, with an addition of blue food with noni juice
819 for *D. sechellia*). Female flies aged 5-8 days after eclosion were used for the
820 experiments.

821 *Sample preparation:* flies were anaesthetized by placing them into an
822 empty vial that was cooled on ice for no longer than ~10 min. Further steps were
823 performed under a dissection microscope, adapting a previous protocol (Silbering
824 et al., 2012). A small drop of blue light-curing glue (595987WW, Ivoclar Vivadent)
825 was placed on top of the copper grid (G220-5, Agar Scientific). Single flies were
826 introduced into the mounting block fixing the back of the fly head to the copper
827 grid with the curing glue. The fly head was slightly bowed down with forceps (to
828 achieve antennal lobe imaging from the dorsal side) while the blue curing light
829 (bluephase C8, Ivovlar Vivadent; placed at least 1 cm from the fly to avoid tissue
830 damage) was focused. We avoided using the wire that was previously used to
831 pull down the antennal plate (Auer et al., 2020; Silbering et al., 2012), as we
832 found that it very frequently damaged the antennal nerves and therefore disrupted
833 central olfactory responses, particularly in *D. sechellia*; the cactus spine and
834 screw previously used to immobilize the fly head were also no longer necessary.
835 An antennal shield (Silbering et al., 2012) was placed over the top of the fly head
836 with the hole positioned centrally, fixed with beeswax to the top of the mounting
837 block. Two-component silicon (Kwik-Sil, World Precision Instruments) was mixed
838 with a toothpick and poured into the hole of the antennal shield to seal the gap
839 between the plate and the fly head, avoiding any leakage onto the antennae. As
840 the silicon was left to harden (during 10-15 min), we used blunt forceps to gently
841 remove silicone on the cuticle on top of the head capsule. A drop of adult
842 hemolymph (AHL) saline (108 mM NaCl, 5 mM KCl, 2 mM CaCl₂, 8.2 mM MgCl₂,
843 4 mM NaHCO₃, 1 mM NaH₂PO₄, 5 mM trehalose, 10 mM sucrose, 5 mM HEPES,
844 pH 7.5) was added into the hole of the antennal shield. Using a blade-splitter, a
845 small rectangular hole was cut in the head cuticle between the eyes and above
846 the antennal plate. Tracheae and glands above the brain were removed with fine
847 forceps. Finally, the brain was rinsed with AHL saline at least 3 times until the
848 antennal lobe appeared clear under the dissection microscope.

849 *Odorant preparation:* serial dilutions of odors were prepared in a fume
850 hood. The solvents used for odor dilutions were different between glomeruli, as
851 some glomeruli were extremely responsive to particular solvents: Or85b/VM5d (2-
852 heptanone (CAS 110-43-0) in dichloromethane (DCM)), Or22a/DM2 (methyl
853 hexanoate (CAS 106-70-7) in paraffin oil), Or59b/DM4 (methyl butyrate (CAS
854 623-42-7) in DMSO (for dose-responses) or paraffin oil (for pulsed stimuli)),
855 Or92a/VA2 (2,3-butanedione (CAS 431-03-8) in paraffin oil). Or85b/VM5d

856 neurons were especially sensitive to odorant contamination, so we prepared a
857 new set of 2-heptanone dilutions when solvent responses started to become
858 evident (approximately every two weeks). Furthermore, before preparing 2-
859 heptanone and methyl butyrate, we washed the odor-containing vial, lid and
860 pipetting tips with DCM and DMSO, respectively. As DCM is highly volatile at
861 room temperature, 2-heptanone/DCM odor dilutions were stored at 4°C.

862 *Image acquisition:* images were acquired using a commercial upright two-
863 photon microscope (Zeiss LSM 710 NLO). An upright Zeiss AxioExaminer Z1 was
864 fitted with a Ti:Sapphire Chameleon Ultra II infrared laser (Coherent) as excitation
865 source. Images were acquired with a 20× water dipping objective (Plan-
866 Apochromat 20× W; NA 1.0), with a resolution of 128×128 pixels (0.8926 pixels
867 μm^{-1}) and a scan speed of 6.30 $\mu\text{s pixel}^{-2}$ (for one-time odor stimulation) or 3.15 s
868 pixel^{-2} (for pulse train odor stimulation). The excitation wavelength was set to 930
869 nm. The output power was modified according to the baseline fluorescence of
870 GCaMP6f, which varied substantially between animals (except for pharmacology
871 experiments, where laser output was consistent to enable comparison of raw
872 fluorescence across animals). The power was set such that the baseline
873 fluorescence was above the detection limit, and that the maximum fluorescence
874 was below saturation, and thereafter unchanged for a given animal. Emitted light
875 was filtered with a 500-550 nm band-pass filter, and photons were collected by an
876 internal detector. Each measurement consisted of 50 images acquired at 4.17 Hz
877 (for one-time odor stimulation) or 8.34 Hz (for pulse train odor stimulation), with
878 stimulation starting ~5 s after the beginning of the acquisition and lasting for 1 s
879 (for one-time odor stimulation) or 200 ms followed by a 200 ms interval repeated
880 ten times (for pulse train odor stimulation).

881 *Olfactory stimulation:* antennae were stimulated using a custom-made
882 olfactometer (Auer et al., 2020; Silbering et al., 2012). In brief, antennae were
883 permanently exposed to air flowing at a rate of 1.5 l min^{-1} by combining a main
884 airstream of humidified room air (0.5 l min^{-1}) and a secondary stream (1 l min^{-1}) of
885 normal room air. Both air streams were generated by vacuum pumps (KNF
886 Neuberger AG) and the flow rate was controlled by two independent rotameters
887 (Analyt). The secondary airstream was guided either through an empty 2 ml
888 syringe or through a 2 ml syringe containing 20 μl of odor or solvent on a small
889 cellulose pad (Kettenbach GmbH) to generate odor pulses. To switch between
890 control air and odor stimulus application, a three-way magnetic valve (The Lee
891 Company, Westbrook, CT) was controlled using MATLAB via a VC6 valve
892 controller unit (Harvard Apparatus). The order of the odor stimuli was always from
893 lower to higher concentrations, preceded by the solvent control. Successive odor
894 stimulations were separated by 1 min intervals.

895 *Pharmacology:* for pharmacological experiments, drugs were diluted in
896 AHL saline to the following final concentrations: 100 μM Picrotoxin (P1675-1G,
897 Sigma-Aldrich, CAS 124-87-8), 50 μM CGP54626 hydrochloride (1088/10,
898 TOCRIS, CAS 149184-21-4), 200 μM (low dose) or 2 mM (high dose),
899 mecamylamine hydrochloride (M9020-5MG, Sigma-Aldrich, CAS 826-39-1).
900 Drugs were applied to the fly after normal recording (“saline / naïve”) by
901 exchanging the AHL saline with drug-diluted saline five times and incubating the
902 preparation for a further 15-40 min before performing further recordings. For
903 mecamylamine application experiments, samples were subsequently washed with
904 AHL saline five times and incubated for 15-40 min, followed by another recording

905 session (“Washed-out”). The lens was meticulously washed with ultrapure water
906 between each session.

907 *Data analyses:* data were processed using Fiji and custom written scripts
908 in R. First, the image stacks were passed through the StackReg plugin (Thevenaz
909 et al., 1998) (transformation: Rigid Body) to correct for movement artefacts. Using
910 Fiji, a circular region of interest (ROI) was set within the glomerulus of interest on
911 the left half of the brain image (except when the signal was weak, in which case
912 the right half of the image was used). The signal intensity averaged across the
913 ROI for each timeframe (hereafter F) was used to calculate the normalized signal

914 $\Delta F/F_0 = \frac{F-F_0}{F_0}$. Here, F_0 (baseline fluorescence) was calculated as the average F

915 during frames 16-19 (1 s before olfactory stimulus onset). The peak $\Delta F/F_0$ value
916 (which represents the odor response intensity) was calculated as the maximum
917 $\Delta F/F_0$ value during frames 20-23 (1 s during olfactory stimulation). We noticed
918 that the maximum $\Delta F/F_0$ value itself was often very different between
919 species/genotypes, presumably due to different expression levels of GCaMP6f.
920 This should, in theory, not affect the normalized $\Delta F/F_0$ value, but we did observe
921 a saturation of neuronal responses above a certain odor concentration, even if
922 the peak $\Delta F/F_0$ value was lower than in other species/genotypes. To compare the
923 dose-response effect between species and genotypes, we further introduced a
924 normalization step. Normalized peak response for each odor dilution (\tilde{p}) was

925 calculated as follows: $\tilde{p} = \frac{p-p_0}{p_{max}-p_0}$. Here, p denotes peak $\Delta F/F_0$ value of a given

926 dilution (median value across animals), p_{max} denotes maximum p among all the
927 dilutions, and p_0 denotes p from the minimum response. Thus, the normalized
928 peak response \tilde{p} takes a value between 0 and 1, where 0 means absence of odor
929 responses and 1 means saturation. This step allowed us to compare the dose-
930 response curve based on the relative response within species and genotypes,
931 regardless of the absolute $\Delta F/F_0$ value. Dynamic ranges were quantified as
932 $p_{max} - p_0$ in each animal rather than taking the median values across animals.

933

934 **Photoactivation**

935 *Animal preparation:* flies of the appropriate genotype (see figure legends) were
936 collected, reared and prepared in the same way as for the two-photon calcium
937 imaging. Female flies aged 6-9 days after eclosion were used for the
938 experiments.

939 *Photoconversion and image acquisition:* the hardware setup was the same
940 as in two-photon calcium imaging. Glomerular location was identified by a brief
941 930 nm scan of the entire antennal lobe. An oval ROI was placed inside the
942 glomerulus of interest, where the ROI was made small enough so that the
943 movement during photoconversion did not result in non-specific labelling. Where
944 non-specific labelling was observed after imaging, data were excluded from
945 further analyses. During photoconversion, the resolution was set to 512×512
946 pixels (3.5704 pixels μm^{-1}) and the scan speed to 0.79 $\mu\text{s pixel}^{-2}$. Excitation
947 wavelength was shifted to 760-780 nm with a power output of 5-15%.
948 Photoconversion was performed by scanning inside the ROI repeatedly (in a
949 single z-plane) for ~15 min. Around 5 min after the beginning of the session, a
950 brief 930 nm scan was performed to check the conversion efficacy and specificity.
951 If photoconversion was weak at this point, we increased the power output. The
952 sample was then placed in a humidified chamber for 30-60 min to allow the
953 diffusion of photoconverted C3PA-GFP. Finally, the fly’s body was removed to

954 reduce motion artefacts and the sample placed again under the two-photon
955 microscope. For imaging, the resolution was set to 1024×1024 pixels (2.3803
956 pixels μm^{-1}) and the scan speed to 1.58-3.15 $\mu\text{s pixel}^{-2}$. The excitation wavelength
957 was shifted back to 930 nm with the power output adjusted to enable visualization
958 of neurite processes. Z-stack images were obtained with a spacing of 1 μm .

959

960 **Electrophysiology**

961 *Single sensillum recordings*: single sensillum electrophysiological recordings were
962 performed essentially as previously described (Auer et al., 2020), using 5-7 day-
963 old female flies, which were grown on standard medium mixed with 0.2 mM all-
964 *trans* retinal (Klapoetke et al., 2014), and, for *D. sechellia*, addition of 10% noni
965 juice. Optogenetic stimulation was performed by exposing one antenna with
966 increasing light intensities via an optic fiber as described in the **Tethered fly**
967 **assay** section (see below). In SPARC2 experiments, ab3 sensilla were identified
968 by location and the use of diagnostic odors. For the data shown in **Fig. 3C**, light-
969 sensitive (experimental group) and non-responding neurons (control) were
970 analyzed. Corrected responses were calculated as the number of spikes in a 0.5
971 s window from the beginning of illumination, subtracting the number of
972 spontaneous spikes in a 0.5 s window 2 s prior to illumination, and multiplying by
973 2 to obtain spikes s^{-1} . Recordings were performed on a maximum of three
974 sensilla per fly. Exact *n* values and mean spike counts for all experiments are
975 provided in **Supplemental Table 1**.

976 *Whole-cell patch clamp recordings*: for *in vivo* VM5d PN recordings, flies
977 were prepared and dissected as previously described (Jeanne and Wilson, 2015).
978 Female flies aged 1-2 days post-eclosion were used for the experiments; one
979 neuron was recorded per brain. The internal patch pipette solution contained 140
980 mM potassium aspartate, 10 mM 4-(2-hydroxyethyl)-1-piperazineethanesulfonic
981 acid, 4 mM MgATP, 0.5 mM Na_3GTP , 1 mM ethylene glycol tetraacetic acid, 1
982 mM KCl and, for cell labelling described below, 13 mM biocytin hydrazide. The pH
983 was adjusted to 7.3, and the osmolarity was adjusted to ~265 mOsm. The
984 external saline contained 103 mM NaCl, 3 mM KCl, 5 mM *N*-tris(hydroxymethyl)
985 methyl-2-aminoethane-sulfonic acid, 8 mM trehalose, 10 mM glucose, 26 mM
986 NaHCO_3 , 1 mM NaH_2PO_4 , 1.5 mM CaCl_2 , and 4 mM MgCl_2 . The osmolarity was
987 adjusted to 270-273 mOsm, and the saline was bubbled with 95% O_2 and 5%
988 CO_2 and reached an equilibrium pH of 7.3. Saline was continuously superfused
989 over the fly during recording. Recordings were acquired with an Axopatch 700B
990 or 200B model amplifier, low-pass filtered at 4 or 5 kHz, and digitized at 10 kHz.
991 Patch pipettes, made from borosilicate glass, were pressure-polished. The
992 estimated final pipette tip opening was less than 1 μm in diameter, and the pipette
993 resistance was 15-45 M Ω .

994 *Olfactory stimulation*: serial dilutions of 2-heptanone (in mineral oil) were
995 freshly prepared before each experiment. A custom-made olfactometer was used
996 to deliver odor to flies. Antennae were consistently exposed to a stream of air at
997 363 ml min^{-1} . Another stream of air (5.3 ml min^{-1}) was directed through a solenoid
998 valve into a 2 ml vial (Thermo Scientific, National C4011-5W) containing either
999 mineral oil alone or an odor solution in mineral oil. Odor delivery, controlled by a
1000 custom MATLAB script and a three-way solenoid valve (The Lee Company,
1001 Westbrook, CT), lasted 2 s. The series of stimuli always started with the solvent
1002 control followed by increasing odor concentrations. Custom-written MATLAB
1003 scripts were used to detect spikes based on the first derivative of the voltage

1004 trace. A threshold was set for each recording and all spikes were visually
1005 inspected to eliminate both false positive and false negative detections. The spike
1006 time was defined as the time of the peak of the first derivative of the voltage
1007 waveform. An average of three trials was taken for each concentration for each
1008 cell. Corrected responses were calculated as the spike rate in a 50 ms (**Fig. 5E**
1009 **and Fig. S7B**) or 500 ms (**Fig. S7B**) window and subtracting the spontaneous
1010 spike rate (computed in a 500 ms window 2 s prior to stimulation). Exact *n* values
1011 and mean spike counts for all experiments are provided in **Supplemental Table 1**.

1012 *Projection neuron backfilling and reconstruction*: each brain was dissected
1013 out of the head capsule after the recording and fixed with 4% PFA (w/v) in PBS
1014 for 20 minutes at room temperature. After washing with PBS-T [PBS with 0.2%
1015 (v/v) Triton X-100 (Sigma Aldrich, #X100)], brains were incubated with
1016 streptavidin Alexa Fluor 568 (1:1000) (Invitrogen S11226) and nc82 (1:50) and
1017 10% Normal Goat Serum in 0.2% PBS-T overnight at RT. The brains were
1018 washed and incubated with streptavidin Alexa Fluor 568 (1:1000) and anti-mouse
1019 Alexa Fluor 633 (1:500) and 10% Normal Goat Serum in 0.2% PBS-T overnight.
1020 After the final wash with PBS, brains were mounted in Vectashield H-1000
1021 (Vector Laboratory, Burlingame, CA) anti-fade mounting medium for confocal
1022 microscopy. Brains were imaged with a Zeiss LSM880 confocal microscope.
1023 Confocal images displayed Biocytin fills in all recordings, and dendritic surface
1024 area was measured using IMARIS 10.0.0 (Bitplane) through a semi-automated
1025 generation of surfaces for each dendritic arbor.

1026 For one *D. melanogaster* recording, the biocytin fill revealed two coupled
1027 cells: one innervating the VM5d glomerulus and the other innervating a different
1028 glomerulus. Correspondingly, two distinct spike waveforms were clearly
1029 discernible in the voltage trace. We excluded this recording from membrane
1030 voltage and input resistance analyses but included it in spike rate analysis
1031 because the VM5d PN spikes could be identified by their clear responses to 2-
1032 heptanone. The VM5d arbor in this fill was included in the dendritic morphology
1033 analysis.

1034

1035 **Tethered fly assay**

1036 *Assay*: the assay was built on a solid breadboard (Thorlabs). The fly tether was
1037 made by inserting and gluing an insect pin (Austerlitz, $\phi = 0.20$ mm) to a 200 μ l
1038 pipette tip, which was mounted on a magnetic articulated stand (NOGA). Two
1039 microphones (lavalier microphone, RODE) were placed ~ 1 mm from the tip of the
1040 wings of the fly, connected to a USB audio interface (Rubix 22, Roland) via TRS-
1041 XLR adaptors (VXLR, RODE). The audio interface was connected to Raspberry
1042 Pi computer (Raspberry Pi 4 1.5 GHz Quad-Core, 8GB RAM), which ran the real-
1043 time feedback program (described below) based on the acoustic inputs. The
1044 output of the feedback system was SPI-connected to a DotStar LED strip (1528-
1045 2488-ND, Adafruit; cut to 30 LEDs), which was bent to make a U-shape that
1046 covers $>180^\circ$ of the fly's horizontal view. The spatial frequency of the visual guide
1047 was set to ~ 0.036 mm⁻¹ (one illumination in every 4 LEDs). The PTFE odor port
1048 was placed at $\sim 30^\circ$ from the right side, facing the fly ~ 1 cm apart to provide
1049 unilateral olfactory stimulation. The suction port was placed at the opposite end of
1050 the odor port, ~ 2 cm from the fly, to stabilize the odor plume. For optogenetic
1051 experiments, single antennae were illuminated using a custom-made optic fiber
1052 (G050UGA, Tubing: FT030, End 1: SMA, End 2: Flat Cleave, Thorlabs), of which
1053 the cleaved end was placed ~ 0.1 mm from one antenna. The position of the optic

1054 fiber was adjusted using a 3D microcontroller (UM-3C, Narishige), and was
1055 monitored by a Pi NoIR camera prior to each session. The fiber was connected to
1056 660 nm fiber-coupled LED (M660FP1, Thorlabs) via a compact LED driver
1057 (LEDD1B, Thorlabs).

1058 *Real-time feedback system:* the feedback system was run by a custom
1059 Python script. The recording was performed binocularly from each wing at the
1060 rate of 44,100 Hz. Each session (20 s) was divided into 0.1 s intervals. The raw
1061 wing beat amplitude ($r_{[L]}$, $r_{[R]}$) was defined by the difference between the
1062 maximum and minimum sound amplitude within each interval. The raw wing beat
1063 was filtered by calculating the median across the three most recent intervals
1064 ($r_{f[L]}$, $r_{f[R]}$). Prior to the experimental session, each fly was calibrated by a “mock”
1065 session, where the visual guide was fixed and the flies beat their wings to obtain
1066 the mean ($\mu_{mock[L]}$, $\mu_{mock[R]}$) and SD ($\sigma_{mock[L]}$, $\sigma_{mock[R]}$) of the filtered wing beat
1067 amplitude as well as the SD of the difference between the left and right wing beat
1068 amplitudes ($\sigma_{mock[L-R]}$). In the experimental sessions, the filtered raw wing beat
1069 amplitudes were standardized using the mean and SD obtained in the mock

1070 session ($z_{[L]} = \frac{r_{f[L]} - \mu_{mock[L]}}{\sigma_{mock[L]}}$, $z_{[R]} = \frac{r_{f[R]} - \mu_{mock[R]}}{\sigma_{mock[R]}}$). The ΔWBA was defined by $z_{[L]} - z_{[R]}$ as a
1071 readout of turning behavior. In each interval, the visual guide was rotated counter-
1072 clockwise (shifting by one adjacent LED) if $\Delta WBA > 3\sigma_{mock[L-R]}$ and clockwise if
1073 clockwise if $\Delta WBA < 3\sigma_{mock[L-R]}$. The $z_{[L]}$, $z_{[R]}$ values were saved after each
1074 session for downstream analyses.

1075 *Animal preparation:* flies of the appropriate genotype were collected
1076 (females and males co-housed). For odor response experiments, females 5-9
1077 days after eclosion were used (except for SPARC2-D-TNT experiments, where
1078 flies were 0-1 day old since the experimental group did not survive for long). For
1079 experiments with apple cider vinegar (Migros, M-Classic), flies were starved for 5-
1080 7 h. Fly rearing for optogenetic experiments is as described in
1081 **Electrophysiology** section. Flies were reared in retinal-containing food for 6-7
1082 days, and females 6-8 days after eclosion were used.

1083 *Sample preparation:* flies were anaesthetized on ice and attached to the fly
1084 tether using blue-curing glue. For optogenetic experiments, fly forelegs were cut
1085 to prevent the flies from perturbing the optic fiber. The fly tether was mounted on
1086 a magnetic stand, and the fly positioned centrally and equidistantly between the
1087 microphones. For optogenetic experiments, videos were taken during positioning
1088 of optic fibers to confirm that the illumination (at intensity 3, as described below)
1089 was confined to one antenna. For SPARC2-D-TNT-HA experiments, as
1090 transgene expression was not detected in a fraction of flies (for unknown
1091 reasons), post-hoc HA immunofluorescence was performed in individual
1092 antennae and/or brains and the behavioral data for animals with positive labelling
1093 in OSN cell bodies and/or axon termini were retained in the downstream
1094 analyses.

1095 *Olfactory stimulation:* odorants (5 ml) were contained in 15 ml Falcon tubes
1096 with two syringe needles pierced at the lid. Tubes were connected to the syringe
1097 needle outlets to provide odor stimulation from the headspace. The flies were
1098 permanently exposed to water vapor at a rate of 0.5 l min^{-1} . A three-way magnetic
1099 valve (The Lee Company, Westbrook, CT) was controlled using MATLAB via a
1100 VC6 valve controller unit (Harvard Apparatus) to switch the airflow from water to
1101 odorants. Either 10 consecutive pulses of 500 ms with 500 ms intervals or a

1102 single 10 s pulse were used as olfactory stimuli. Noni juice was diluted in water
1103 while benzaldehyde was diluted in paraffin oil.

1104 *Optogenetic stimulation:* LED illumination was controlled by sending TTL
1105 signals to the LED driver. 10 consecutive pulses of 500 ms with 500 ms intervals
1106 were used. The intensity of the illumination was modified by the dial on the LED
1107 driver, which could be modulated from intensity 0 (mock-stimulation) to 6
1108 (maximum). Intensity 4 was used for stimulation in most experiments, except for
1109 low-intensity stimulation (intensity 3) to match the OSN spike rate with SPARC2-
1110 D-CsChrimson experiments. For SPARC2-D-CsChrimson experiments, we
1111 noticed that the animals either displayed expression of CsChrimson (as
1112 detectable by the Venus tag) in about half of the Or22a OSN population or had no
1113 expression at all. The reason for this heterogeneity is unknown but we performed
1114 post-hoc imaging of Venus fluorescence in individual antennae of all animals to
1115 analyze data from only those that expressed the transgene.

1116 *Data analyses:* data were analyzed with custom programs in R. The
1117 quantification was performed in 1 s time windows corresponding to pre-stimulus
1118 baseline (4-5 s) and individual odor-pulse responses (1st peak: 5-6 s, 2nd peak: 6-
1119 7 s, ..., 10th peak: 14-15 s). For quantification of ΔWBA in each time window, the
1120 ΔWBA values above the 50% quantile were used, to avoid picking outliers and
1121 non-attractive epochs.

1122

1123 **Wind tunnel assay**

1124 Free flight tracking was performed in a 1 m × 0.5 m × 0.5 m wind tunnel housed in
1125 a temperature- and humidity-controlled room (22°C, 60% RH). The wind tunnel
1126 floor was illuminated by blue LEDs underneath a light-diffusive film that lined the
1127 tunnel floor, overlaid with a grid of infrared transmissible film; this grid formed a
1128 checkerboard-like lattice on the floor to provide flies with ventral optic flow
1129 information. The walls of the wind tunnel tapered from blue on the floor to black
1130 along the ceiling. Along the top of the wind tunnel were two white LED strips, to
1131 provide sufficient orange light for *Drosophila* photoreceptor re-isomerization (Byk
1132 et al., 1993). Total illumination in the wind tunnel was 452 Lux as measured from
1133 the wind tunnel center (LX1330B light sensor, Dr. Meter).

1134 Fly tracking was performed with 12 synchronized Basler acA720 cameras
1135 (Basler AG, Ahrensburg) recording at 100 Hz (**Fig. S4A**). The walls and floor of
1136 the wind tunnel were homogeneously illuminated with arrays of infrared LEDs, and
1137 cameras were outfitted with IR pass filters to track flies using only infrared
1138 wavelengths. Tracking was performed using Braid software (Straw et al., 2011).
1139 Odor plumes were introduced in the wind tunnel through an odor port constructed
1140 from a 20 cm tall rigid acrylic tube that had a 90° bend towards the top so that its
1141 outward facing opening was parallel to the wind (**Fig. S4B**). The odor port was
1142 installed on the far upwind end of the tunnel and its open face was covered by an
1143 aluminum mesh to prevent flies from entering the odor plumbing. Plumes were
1144 generated by fluxing air through a mass flow controller (Alicat Scientific, Tuscon)
1145 at 200 cm³ min⁻¹. The air was then bubbled into 150 ml noni juice at the bottom of
1146 a jar and subsequently through tubing leading to the odor port in the wind tunnel.

1147 For wind tunnel experiments we used 3-7 day old female flies. 15 animals
1148 were collected in the morning and starved by placing them into a tube containing
1149 a moist Kimwipe for 8 h. The flies were placed in the wind tunnel with a 40 cm s⁻¹
1150 air flow and tracking initiated. Flies were allowed to fly about the wind tunnel
1151 volume for 16-20 h before the recording was terminated the following day.

1152 *Data analyses:* data were analyzed using Python (v3.11). We first filtered
1153 out all trajectories from flies that were walking on the tunnel floor or ceiling to
1154 focus analyses on flying animals. Our trajectory inclusion criteria were: (i) >500
1155 ms long; (ii) >10 cm in the horizontal plane; (iii) a median position of >5 cm away
1156 from any of the tunnel walls; (iv) passed within a 10 cm radius of where the odor
1157 plume was aligned in the y-z plane (this excluded flies that simply transited the
1158 wind tunnel along the ceiling, far away from the plume).

1159 To analyze the radial distance from the plume, we binned the point cloud
1160 generated by all trajectories into 5 cm thick cross-sections, beginning 5 cm
1161 downwind of the plume source. We then pared the point cloud further to 10 cm
1162 above and below the plume ($0.1 < z < 0.3$) to isolate trajectory portions that were
1163 most likely interacting with the plume (**Fig. S4E**), for analyses with or without this
1164 restriction. Based on the occupancy maps of trajectories in space from both wild-
1165 type *D. sechellia* and *D. melanogaster*, we assumed that the plume sank by 5 cm
1166 from the odor nozzle to the end of the wind tunnel and calculated the plume
1167 centerline using this mode (for comparisons of straight versus sloped plume
1168 models see **Fig. S4E-F**). From each of the segmented point clouds we report the
1169 mean as the mean of all points, independent of trajectories that contributed to
1170 them. Results were robust to whether we instead analyzed each trajectory as an
1171 independent sample. For course direction distributions, we included only the point
1172 cloud within a 3 cm radius of our estimated plume volume and calculated the
1173 kernel densities of the course direction of all points within the estimated plume
1174 volume. We further divided the data to the point cloud in the downwind half of the
1175 wind tunnel, where trajectories typically began, and the upwind half of the wind
1176 tunnel, terminating 5 cm downwind of the plume's origin.

1177

1178 **Statistics and reproducibility**

1179 Data were analyzed and plotted using Excel, R (v3.2.3; R Foundation for
1180 Statistical Computing, Vienna, Austria, 2005; R-project-org), MATLAB (2023a),
1181 GraphPad Prism (10.1.1) and Python (v3.11).

1182

1183 **Data, code and biological material availability**

1184 All relevant data supporting the findings of this study are included as source data
1185 or available from the corresponding authors upon request. Code used for
1186 analyses and all unique biological materials generated in this study are available
1187 from the corresponding authors upon request.

1188 **Figure Legends**

1189

1190 **Figure 1: Selective expansion of noni-sensing olfactory sensory neuron**
1191 **populations is a complex developmental trait.**

1192 **(A)** *D. sechellia* specializes on noni fruit compared to the generalists *D. simulans*
1193 and *D. melanogaster*. Ma, million years ago.

1194 **(B)** Left top, schematic of the drosophilid third antennal segment covered by
1195 sensilla of diverse morphological classes and housing the sacculus. Left bottom,
1196 antennal basiconic 3 (ab3) sensilla house two neurons expressing the odorant
1197 receptor Or22a (and Or22b in *D. melanogaster* and *D. simulans*; this paralog is
1198 lost in *D. sechellia*) in the A neuron (hereafter, “Or22a neuron”) and Or85c/b in
1199 the B neuron (both paralogs are co-expressed; hereafter, “Or85b neuron”). Right,
1200 antennal *Or22a/(b)* and *Or85b* expression in *D. sechellia* (*Drosophila* Species
1201 Stock Center (DSSC) 14021-0248.07, females) and *D. simulans* (DSSC 14021-
1202 0251.004, females). Scale bar, 25 μ m. In addition to ab3 sensilla (dashed line),
1203 Or85b is expressed in ~10 spatially-segregated OSNs in ab6 sensilla in all three
1204 species (**Fig. S1B**).

1205 **(C)** Comparison of olfactory sensilla numbers in *D. melanogaster* (Canton-S), *D.*
1206 *simulans* (DSSC 14021-0251.004) and *D. sechellia* (DSSC 14021-0248.07) (all
1207 females) as assessed by RNA FISH using a diagnostic *Or* probe (grey
1208 background) for each sensillum class. Data for Ir-expressing coeloconic sensilla
1209 and sacculus chamber 3 (sac3) neurons are from (Prieto-Godino et al., 2017);
1210 Ir75d neurons common to ac1, ac2 and ac4 sensilla are not shown. In this and all
1211 following panels, box plots show the median and first and third quartiles of the
1212 data, overlaid with individual data points. Wilcoxon signed-rank test with
1213 comparison to *D. melanogaster*. NS, not significant ($P > 0.05$); * $P < 0.05$; ** $P <$
1214 0.01 ; *** $P < 0.001$.

1215 **(D)** Reciprocal hemizygoty test of the *Or22a/(b)* and *Or85c/b* loci for
1216 contributions to species-specific OSN numbers in *D. simulans/D. sechellia*
1217 hybrids. Using RNA FISH to quantify numbers of *Or22a/(b)* and *Or85b* expressing
1218 OSNs in the indicated genotypes (“*Dsec +*” = *D. sechellia.07* wild-type, “*Dsim +*” =
1219 *D. simulans.04* wild-type, “*Dsec -*” = *DsecOr22a^{RFP}* or *DsecOr85b^{GFP}*, “*Dsim -*” =
1220 *DsimOr22a/b^{RFP}* or *DsimOr85b^{GFP}*), no allele-specific expression differences were
1221 observed at either locus. Wilcoxon signed-rank test with comparison to wild-type
1222 hybrids. NS, not significant ($P > 0.05$).

1223 **(E)** Quantification of GFP-expressing neurons in antennae of *DsecOr85b^{GFP}*,
1224 *DsimOr85b^{GFP}* and F1 hybrid males and females, and in the F2 progeny of the
1225 backcrosses of F1 hybrid females to either parental strain. The black line
1226 indicates the mean cell number.

1227 **(F)** Logarithm of odds (LOD) score across all four chromosomes for loci impacting
1228 Or85b neuron numbers based on the phenotypic data in **e**. Dashed horizontal
1229 lines mark $P = 0.05$; non-dashed horizontal lines mark $P = 0.01$.

1230 **(G)** Effect sizes for the significant QTL intervals on chromosome 3 and X in the *D.*
1231 *simulans* backcross. A, *D. simulans* allele; B, *D. sechellia* allele. A candidate
1232 gene, *lozenge* – encoding a transcription factor involved in sensilla specification
1233 development (Gupta et al., 1998) – that is located directly below the highest score
1234 of our trait map on the X chromosome, did not affect OSN numbers (**Fig. S2E-I**).

1235

1236

1237

1238

1239

Figure 2: Persistent behavioral tracking of noni odors in *D. sechellia*.

1240

(A) Schematic of the tethered fly behavioral assay. ΔWBA : left-right difference of standardized wing beat amplitudes (see **Methods** for details), TTL: Transistor-transistor logic.

1241

1242

1243

1244

1245

1246

1247

1248

1249

1250

(B) Odor-tracking behavior towards noni juice and control stimuli (H_2O) in wild-type *D. sechellia* (DSSC 14021-0248.07) and *D. melanogaster* (CS) flies. Left, time course of ΔWBA (mean \pm SEM) where black bars indicate the timing of odor stimulation (ten 500 ms pulses with 500 ms intervals). Right, quantification in 1 s time windows immediately prior to stimulus onset (“pre”) and thereafter corresponding to individual stimulus pulses (“1-10”). Mean \pm SEM are shown (raw data are provided in the Source Data). Paired *t*-test *** $P < 0.001$; ** $P < 0.01$; * $P < 0.05$, otherwise $P > 0.05$. $n = 30$ animals each.

1251

1252

1253

(C) Odor-tracking behavior towards noni juice in *D. sechellia* *Or* and *Ir* mutants. Paired *t*-test, *** $P < 0.001$; ** $P < 0.01$; * $P < 0.05$, otherwise $P > 0.05$. $n = 30$ animals each.

1254

1255

1256

1257

1258

1259

1260

1261

1262

(D) Left, example trajectories (black lines) in the x-y plane of *D. sechellia* (DSSC 14021-0248.07), *D. melanogaster* (a hybrid *Heisenberg-Canton-S* (*HCS*); our CS strain exhibited poor flight performance in this assay) and *D. sechellia* *Or22a*^{RFP} mutants flying in the presence of a noni plume (origin at the orange dot). Right, occupancy heat maps of trajectories that came at least once within 10 cm of the plume centerline for *D. melanogaster* ($n = 1346$ trajectories, 4 recording replicates, 60 flies), *D. sechellia* wild-type ($n = 835$ trajectories, 7 recording replicates, 105 flies) and *D. sechellia* *Or22a*^{RFP} mutants ($n = 509$ trajectories, 6 recording replicates, 90 flies).

1263

1264

1265

1266

1267

1268

1269

1270

(E) Annotated view of the wild-type *D. sechellia* trajectories (from **(D)**) illustrating the data analyses performed in **(F,G)**. Based upon the trajectory distribution, we inferred that the noni juice plume sank by ~ 5 cm from the odor nozzle to the end of the tracking zone in the wind tunnel; this is likely due to the odor-laden air’s higher water content (and so higher density) than the surrounding air. We therefore estimated the plume center as a line connecting the nozzle and a point 5 cm lower in the z-axis at the end of the wind tunnel. Our results are qualitatively robust whether or not we account for plume sinking (**Fig. S4D-F**).

1271

1272

1273

1274

1275

(F) Mean radial distance of the point cloud from the plume centerline for the trajectories in **(D)**. Data were binned into 5 cm y-z plane cross-sections starting 5 cm downwind from the plume origin and restricted to 10 cm altitude above or below the estimated plume model. Non-parametric bootstrapped comparison of medians $P < 0.001$.

1276

1277

1278

1279

1280

1281

1282

1283

1284

1285

(G) Kernel density of the course direction distribution of points within a 3 cm radius of the plume centerline (orange circle on cross-section in **(E)**), further parsed into the point cloud in the downwind or upwind halves of the wind tunnel (see **(E)**). Downwind half kernels: *D. melanogaster* (20,912 points from 511 unique trajectories), *D. sechellia* wild-type (15,414 points from 367 trajectories), *D. sechellia* *Or22a*^{RFP} (3,244 points from 164 unique trajectories). Upwind half kernels: *D. melanogaster* (80,594 points from 615 unique trajectories), *D. sechellia* wild-type (136,827 points from 501 unique trajectories), *D. sechellia* *Or22a*^{RFP} (40,560 points from 286 unique trajectories).

1286

Figure 3: Behavioral significance of OSN number.

1287 **(A)** Optogenetic stimulation of Or22a OSNs in *D. melanogaster* (top) and *D.*
1288 *sechellia* (bottom). Left, expression of CsChrimson in the antenna detected by
1289 expression of the Venus tag. Scale bar, 20 μ m. Middle, single-sensillum
1290 recordings of Or22a OSNs in response to optogenetic stimulation of CsChrimson-
1291 expressing and control sensilla. The red line links the mean neuronal response at
1292 each light intensity, overlaid with individual data points. The black frame indicates
1293 the light intensity used for behavioral experiments. $n = 5-10$ sensilla (exact
1294 numbers are listed in **Supplemental Table 1**), unpaired Student's *t*-test, *** $P <$
1295 0.001 ; * $P < 0.05$, otherwise $P > 0.05$. Right, behavioral responses of the same
1296 genotypes in response to red light stimulation (ten 500 ms pulses with 500 ms
1297 intervals, indicated by the red bars). Paired *t*-test, ** $P < 0.01$; * $P < 0.05$,
1298 otherwise $P > 0.05$. $n = 29$ (*D. melanogaster*) and 30 (*D. sechellia*) animals.
1299 Genotypes: *D. melanogaster* *w;UAS-CsChrimson-Venus/+* (control), *w;UAS-*
1300 *CsChrimson-Venus/Or22a-Gal4* (experimental), *D. sechellia* *w;;UAS-*
1301 *CsChrimson-Venus/+* (control), *w;Or22a^{Gal4}/+;UAS-CsChrimson-Venus/+*
1302 (experimental).
1303 **(B)** Behavioral responses of *D. sechellia* upon optogenetic stimulation of Or22a
1304 OSNs (top) and to noni odor stimulation (middle), in the same animals. Bottom,
1305 comparison of Δ WBA between light and odor responses. Paired *t*-test, *** $P <$
1306 0.001 , ** $P < 0.01$, * $P < 0.05$, otherwise $P > 0.05$. $n = 27$ animals each. Genotype
1307 as in **(A)**.
1308 **(C)** Sparse activation of *D. sechellia* Or22a OSNs. Left, expression of
1309 CsChrimson in an antenna of *D. sechellia* expressing *UAS-SPARC2-D-*
1310 *CsChrimson-Venus* in Or22a OSNs. Fluorescent labelling was sparser than in
1311 *UAS-CsChrimson-Venus* expressing animals, but the dense packing of
1312 membrane-labelled neurons prevented quantification. Experiments in *D.*
1313 *melanogaster* (**Fig. S6B**) and with the *UAS-SPARC2-D-TNT-HA* transgene
1314 (below) support expression in ~50% of Or22a OSNs with this SPARC version.
1315 Scale bar, 20 μ m. Middle, single-sensillum recordings of Or22a OSNs in
1316 response to optogenetic stimulation. ab3 sensilla were first identified by
1317 stimulation with diagnostic odors (not shown); responses of CsChrimson-
1318 expressing neurons (experimental group) and non-expressing neurons (control,
1319 often from the same animal) are shown. $n = 8-9$ (exact numbers are listed in
1320 **Supplemental Table 1**), unpaired *t*-test, *** $P < 0.001$; * $P < 0.05$, otherwise $P >$
1321 0.05 . Right, *D. sechellia* behavior upon optogenetic activation of about half of
1322 their Or22a expressing neurons. Paired *t*-test, *** $P < 0.001$; * $P < 0.05$; otherwise
1323 $P > 0.05$. $n = 26$ animals. Genotypes: *D. sechellia* *w;Or22a^{Gal4}/UAS-SPARC2-D-*
1324 *CsChrimson-Venus;;nSyb- Φ C31/+*.
1325 **(D)** Sparse inhibition of *D. sechellia* Or22a OSNs. Left, HA immunofluorescence
1326 in an antenna of *D. sechellia* (females) expressing *UAS-SPARC2-D-TNT-HA* in
1327 Or22a OSNs. Scale bar, 20 μ m. Quantification of cell-labelling is shown below.
1328 Middle, *D. sechellia* odor-tracking behavior towards noni juice of flies in effector
1329 control (top), driver control (middle), or in experimental animals with blocked
1330 synaptic transmission in approximately half of their Or22a neurons (bottom).
1331 Paired *t*-test, *** $P < 0.001$; ** $P < 0.01$; * $P < 0.05$; otherwise $P > 0.05$. $n = 34$
1332 animals each. Genotypes: *D. sechellia* *w;UAS-SPARC2-D-TNT-HA-GeCO/+;;+/+*
1333 (effector control), *D. sechellia* *w;Or22a^{Gal4}/+;;nSyb- Φ C31/+* (driver control), *D.*
1334 *sechellia* *w;Or22a^{Gal4}/UAS-SPARC2-D-TNT-HA-GeCO;;nSyb- Φ C31/+*
1335 (experimental group).
1336

1337 **Figure 4: Increased sensory and synaptic pooling in noni-sensing**
1338 **glomeruli.**

1339 **(A)** Schematic of OSN-PN connectivity in the antennal lobe. Or22a OSNs
1340 (orange) and Or85b OSNs (blue) have cell bodies in the antenna and axons
1341 projecting to the DM2 and VM5d glomerulus, respectively. The soma of second-
1342 order PNs (green) are located in three distinct clusters around the antennal lobe
1343 (ad, anterodorsal; l, lateral; v, ventral); these neurons synapse with OSNs (the
1344 majority constrained to a single glomerulus) and send axonal projections to higher
1345 olfactory centers. For clarity, LN are not illustrated (see text)

1346 **(B)** Transgenic labelling of PNs in the *D. sechellia* antennal lobe using the
1347 *VT033006-Gal4* or *VT033008-Gal4* drivers to express *UAS-GCaMP6f* (here used
1348 simply as a fluorescent reporter). Immunofluorescence on whole-mount brains
1349 was performed with antibodies against GFP (detecting GCaMP6f) and nc82
1350 (labelling the synaptic protein Bruchpilot (Wagh et al., 2006)). The VM5d
1351 glomerulus is demarcated by a white line in the *VT033008-Gal4* line. Scale bar,
1352 25 μm .

1353 **(C)** Left, representative image of VM5d PNs labelled by photo-activatable GFP
1354 (PA-GFP) in *D. melanogaster* and *D. sechellia*. Genotypes: *D. melanogaster*
1355 *UAS-C3PA-GFP/+;UAS-C3PA-GFP/VT033008-Gal4* (for VM5d PNs) or *UAS-*
1356 *C3PA-GFP/+;UAS-C3PA-GFP/VT033006-Gal4* (for DM2 PNs); *D. sechellia* *UAS-*
1357 *C3PA-GFP/VT033008-Gal4* (for VM5d PNs) or *UAS-C3PA-GFP/VT033006-Gal4*
1358 (for DM2 PNs). Arrows indicate the PN cell bodies; faint background GFP signal
1359 in other soma are irrelevant neuron types. The antennal lobe (AL) is demarcated
1360 by a dashed line. Scale bar, 25 μm . Right, quantification of Or22a and Or85c/b
1361 PN numbers innervating the DM2 and VM5d glomeruli, respectively, by labelling
1362 with PA-GFP (using two different driver lines for VM5d PNs) in *D. sechellia* and *D.*
1363 *melanogaster*. Mann-Whitney *U*-test, NS, not significant. $P > 0.05$.

1364 **(D)** Visualization of antennal lobe glomeruli by expression of the $D\alpha 7$ -GFP post-
1365 synaptic marker in PNs. Genotypes: *D. melanogaster* *w;VT033006-Gal4/UAS-*
1366 *D\alpha 7-GFP*; *D. sechellia* *w;VT033006-Gal4/+;UAS-D\alpha 7-GFP/+*. Scale bar, 20 μm .

1367 **(E)** Quantification of the volumes of DM2, VM5d and a control glomerulus, DM6
1368 (innervated by Or67a neurons) in *D. sechellia* and *D. melanogaster* (females).
1369 Wilcoxon signed-rank test. $**P < 0.005$; $***P < 0.001$.

1370 **(F)** Representative images of single dye-labelled VM5d PNs in *D. melanogaster*
1371 and *D. sechellia*. Genotypes: *D. melanogaster* *w;VM5d-Gal4/UAS-GFP*, *D.*
1372 *sechellia* *w;VM5d-Gal4/UAS-myrGFP* (the GFP fluorescence is not shown). Scale
1373 bar, 5 μm . Right, quantification of VM5d PN dendrite surface area and volume.
1374 Student's *t*-test. $*P < 0.05$.

1375 **(G)** Left, representative images of post-synaptic puncta in VM5d, DM2 and DM6
1376 PNs labelled by $D\alpha 7$ -GFP in *D. melanogaster* and *D. sechellia* (genotypes as in
1377 **(D)**). Scale bar, 5 μm . Right, quantification of the number of post-synaptic puncta
1378 in these glomeruli. Wilcoxon signed-rank test. $**P < 0.005$; $***P < 0.001$.

1379
1380 **Figure 5: Sustained representation of noni odor stimuli in PNs of *D.***
1381 ***sechellia*.**

1382 **(A-D)** Whole-cell patch clamp recording from VM5d PNs in *D. melanogaster* and
1383 *D. sechellia*; the glomerular circuit is schematized on the left. Genotypes as in
1384 **Fig. 4F. (A)** Voltage trace of VM5d PNs in response to a pulse of 2-heptanone.
1385 **(B-D)**, Comparison of input resistance **(B)**, resting membrane potential **(C)**, and

1386 spontaneous activity **(D)** between *D. melanogaster* and *D. sechellia*. Student's *t*-
1387 test. ***P* < 0.01. *n* = 4-5.

1388 **(E)** Dose-response relationship of VM5d PN firing to 2-heptanone. Quantification
1389 of spike frequency was performed in a 50 ms window covering the peak
1390 response. Student's *t*-test. ***P* < 0.01, **P* < 0.05. *n* = 2-5 animals (exact numbers
1391 and mean responses are listed in **Supplemental Table 1**). EC₅₀ values [Log] are
1392 as follows: -7.46 (*Dmel*), -6.87 (*Dsec*).

1393 **(F)** VM5d PN spike frequency in response to 10⁻⁶ dilution of 2-heptanone. Left,
1394 time course of spike frequency. Mean ± SEM are shown. Right, quantification of
1395 the decay magnitude (i.e. start (first 50 ms) - end (last 500 ms before odor
1396 offset)). Student's *t*-test. **P* < 0.05. *n* = 5 animals each.

1397 **(G-H)** Dose-dependent, odor-evoked calcium responses in Or85b/VM5d **(G)** and
1398 Or22a/DM2 **(H)** OSN axon termini and PN dendrites in the antennal lobe of *D.*
1399 *melanogaster* and *D. sechellia*, reported as normalized GCaMP6f fluorescence
1400 changes. Plots are based on the data in **Fig. S8**. EC₅₀ values [Log] are as follows:
1401 Or85b OSNs: -6.50 (*Dmel*), -6.51 (*Dsec*); VM5d PNs: -7.82 (*Dmel*), -7.87 (*Dsec*);
1402 Or22a OSNs: -7.42 (*Dmel*), -8.23 (*Dsec*); DM2 PNs: -7.97 (*Dmel*), -9.61 (*Dsec*).
1403 Genotypes are as follows. OSN calcium imaging: *D. melanogaster* UAS-
1404 GCaMP6f/Orco-Gal4,UAS-GCaMP6f, *D. sechellia* UAS-GCaMP6f/UAS-
1405 GCaMP6f;+/DsecOrco^{Gal4}. PN calcium imaging: *D. melanogaster* UAS-
1406 GCaMP6f/+;+/VT033008-Gal4 (for VM5d PNs), *D. melanogaster* UAS-
1407 GCaMP6f/+;+/VT033006-Gal4 (for DM2 PNs), *D. sechellia* UAS-
1408 GCaMP6f/VT033008-Gal4 (for VM5d PNs), UAS-GCaMP6f/VT033006-Gal4 (for
1409 DM2 PNs).

1410 **(I)** Responses of Or85b OSNs to pulsed odor stimuli (ten 200 ms pulses, each
1411 separated by 200 ms, as indicated by the black bars). For both species, left
1412 panels show the time course (mean ± SEM Δ*F*/*F*₀) and right panels show the
1413 quantification of Δ*F*/*F*₀ peak to the 1st and 10th stimulation. Paired *t*-test. ** *P* <
1414 0.01, * *P* < 0.05. *n* = 8 animals each.

1415 **(J-K)** Pulsed odor responses of VM5d PNs **(J)** and DM2 PNs **(K)**. Paired *t*-test, **
1416 *P* < 0.01. *n* = 8 animals each.

1417 **(L-M)** Pulsed odor responses of VA2 (Or92a) and DM4 (Or59b) PNs (two control
1418 pathways where the number of cognate OSNs is conserved between species
1419 **(Fig. 1C)**). Paired *t*-test. *** *P* < 0.001; ** *P* < 0.01. *n* = 6 animals each. Dose
1420 response data for these neurons are provided in **Fig. S11**. Genotypes are as for
1421 DM2 PN imaging in **(H)**.

1422
1423 **Figure 6: Mechanisms of sustained PN responses in *D. sechellia*.**

1424 **(A)** Odor pulse responses of VM5d PNs following application of a GABA
1425 antagonist. PN responses in normal AHL saline (left) or containing 100 μM
1426 picrotoxin + 50 μM CGP54626 (right). Paired *t*-test, *** *P* < 0.001, NS *P* > 0.05. *n*
1427 = 8 animals each. Genotypes are indicated in **Fig. 5G** legend.

1428 **(B)** Odor pulse responses of VM5d PNs following application of low doses (200
1429 μM) of mecamylamine (nAChR antagonist) to weakly block cholinergic inputs. *D.*
1430 *melanogaster* and *D. sechellia* PN responses in normal AHL saline,
1431 mecamylamine and AHL saline wash-out. Paired *t*-test. *** *P* < 0.001, * *P* < 0.05,
1432 NS *P* > 0.05. *n* = 7 animals each.

1433 **(C)** Odor pulse responses of *D. sechellia* VM5d PNs in intact (top) and right
1434 antenna-ablated (bottom) animals, in which the OSN input is halved. Paired *t*-test,
1435 * *P* < 0.05, NS *P* > 0.05. *n* = 7 each.

1436 **(D)** Model illustrating the complementary effects of OSN sensitization (due to
1437 receptor tuning) and reduced PN decay magnitude (putatively due to OSN
1438 population increases; see **Discussion**) on odor-evoked activity, which might
1439 synergize to promote sensitive and persistent long-range odor tracking toward the
1440 noni host fruit by *D. sechellia*, but not *D. melanogaster*.
1441

1442 **Supplemental Figure Legends**

1443

1444 **Figure S1: Investigation of potential mechanisms underlying ab3 sensilla**
1445 **expansion.**

1446 **(A)** Quantification of *Or22a/(b)* RNA expressing OSNs in the antenna of six *D.*
1447 *sechellia*, *D. simulans* and *D. melanogaster* strains. For strain details see
1448 **Supplemental Table 2**. Wilcoxon signed-rank test, *P* values adjusted for multiple
1449 comparisons using the Benjamini and Hochberg method. Comparisons to *Dsec07*
1450 (genetic background of transgenic lines) are shown. NS, not significant ($P > 0.05$);
1451 $**P < 0.01$; $***P < 0.001$.

1452 **(B)** Top, immunofluorescence for GFP and RNA FISH for *Or85b* on whole-mount
1453 antennae from *D. melanogaster Or49b-GFP* animals. Arrowheads indicate paired
1454 neurons. *Or85b* neurons are housed in ab3 (with *Or22a* neurons) and ab6
1455 sensilla (with *Or49b* neurons), but only the ab3 population is expanded in *D.*
1456 *sechellia* (**Fig. 1C**). Scale bar, 25 μm .

1457 **(C)** Comparison of the number of *Or22a* RNA-expressing OSNs in the antenna of
1458 *D. sechellia* raised on (left) and without (right) noni supplement. Scale bar, 25 μm .
1459 Quantification to the right. Wilcoxon rank-sum test. NS, $P > 0.05$.

1460 **(D)** Top left, schematic of the ab2 sensillum housing *Or59b* and *Or85a* neurons.
1461 Top right, RNA FISH for *Or59b* on whole-mount antennae from *D. melanogaster*,
1462 *D. simulans* and *D. sechellia* wild-type animals (females). Scale bar, 25 μm .

1463 **(E)** Top, schematic of developmental transitions from larval antennal disc to adult
1464 antenna. Schematic of the larval antennal disc, within which concentric arcs of
1465 sensory organ progenitors (SOPs) are specified, each of which gives rise to a
1466 sensillum. Different SOP types have a stereotyped developmental origin in a
1467 given arc (adapted from (Chai et al., 2019)). Arrows indicate the change in
1468 relative population size in *D. sechellia* compared to *D. melanogaster*. No obvious
1469 relationship between ab3 number increase and compensatory reduction in
1470 sensilla derived from SOPs in the same or neighboring arcs is evident.

1471 **(F)** Representative pictures of the reciprocal hemizyosity test at the *Or22a/b* and
1472 *Or85c/b* loci using RNA FISH results shown in **Fig. 1D**. Schematics on top
1473 indicate expression from the respective alleles.

1474

1475 **Figure S2: Genetic analysis of OSN cell number expansion.**

1476 **(A)** Left, schematics depicting the introduction of a nuclear-localized GFP reporter
1477 (GFPnls) at the *Or85b* locus of *D. sechellia* and *D. simulans* via CRISPR/Cas9
1478 genome engineering. Right, GFP signal in antennae of *DsecOr85b^{GFP}* and
1479 *DsimOr85b^{GFP}* animals. Scale bar, 25 μm .

1480 **(B)** Immunofluorescence for GFP and *Or22a* RNA FISH on whole-mount
1481 antennae from *DsecOr85b^{GFP}* animals. Arrowheads indicate neighboring neurons.
1482 Scale bar, 25 μm .

1483 **(C)** Introgression of chromosomal fragments marked with a transgenic RFP
1484 marker (dashed line) from *D. sechellia* into *D. simulans* spanning varying extents
1485 of the QTL peak on chromosome 3.

1486 **(D)** Left, quantification of GFP-expressing neurons in F2 backcrosses of the *D.*
1487 *sechellia* RFP transgenic line to *D. simulans Or85b^{GFP}* flies comparing RFP
1488 positive and negative siblings (females only). Right, quantification of GFP-
1489 expressing neurons in the five *D. sechellia* introgression lines depicted in **(A)**
1490 comparing RFP positive and negative siblings. *n* are listed in the figure. Wilcoxon
1491 signed-rank test. NS, not significant ($P > 0.05$); $*P < 0.05$; $***P < 0.001$.

1492 (E) Left, location of the *lozenge* (*lz*) gene (dashed line) relative to the QTL peaks
1493 detected on the X chromosome. Right, schematics depicting the *lozenge* gene
1494 organization and the structure of mutant alleles in both *D. sechellia* and *D.*
1495 *simulans*. The fluorescent marker was integrated into the first coding exon.
1496 (F) Comparison of antennal morphology in wild-type and *lz* mutant *D. sechellia*
1497 and *D. simulans*. In both species, loss of *lz* results in a lack of basiconic sensilla
1498 (white arrowheads) compared to wild-type, similar to *D. melanogaster lz* mutants
1499 (Gupta et al., 1998). Scale bar, 25 μm ; inset scale bar, 5 μm .
1500 (G) Quantification of GFP-expressing neurons in *Dsimlz*^{RFP} heterozygote mutant
1501 and wild-type siblings (females only). Wilcoxon signed-rank test. ** $P < 0.01$.
1502 (H) Quantification of GFP-expressing neurons in *DsecIz*^{RFP} heterozygote mutant
1503 and wild-type siblings (females only). Wilcoxon signed-rank test. *** $P < 0.001$.
1504 (I) Quantification of GFP-expressing neurons in *trans*-heterozygote hybrid siblings
1505 (females only) carrying either a *DsecIz*^{RFP} or *Dsimlz*^{RFP} allele. Wilcoxon signed-
1506 rank test. NS, not significant ($P > 0.05$).
1507 (J) Quantification of Ir75b neurons in wild-type *D. sechellia* (DSSC 14021-
1508 0248.25) and *D. simulans* (DSSC 14021-0251.195) (mixed genders) and
1509 respective F2 progeny derived from backcrosses of F1 hybrid females to either
1510 parental strain (mixed genders). The black line indicates the mean cell number.
1511 (K) Logarithm of odds (LOD) score across all four chromosomes for loci
1512 impacting Ir75b neuron numbers based on phenotyping data shown in J. Dashed
1513 horizontal lines mark $P = 0.05$; non-dashed horizontal lines mark $P = 0.01$.

1514
1515 **Figure S3: Odor-tracking behavior of wild-type strains.**

1516 (A) Odor-tracking behavior towards noni juice in other wild-type strains of *D.*
1517 *sechellia* and *D. melanogaster* (see **Supplemental Table 2**), plotted as in **Fig.**
1518 **2B**. Paired *t*-test, *** $P < 0.001$; ** $P < 0.01$; * $P < 0.05$; otherwise $P > 0.05$. $n = 30$
1519 (*DmelBK*, *DmelrHR*, *Dsec19*, *Dsec31*) or 27 (*DmelOR*, *Dsec28*) animals.
1520 (B) Odor-tracking behavior towards apple cider vinegar in wild-type *D. sechellia*
1521 strains. Paired *t*-test, *** $P < 0.001$; ** $P < 0.01$; * $P < 0.05$; otherwise $P > 0.05$. n
1522 = 30 animals each.

1523
1524 **Figure S4: Odor tracking in a wind tunnel.**

1525 (A) Array of 12 tracking cameras above the wind tunnel used for 3D tracking of
1526 flies in the presence of a noni plume.
1527 (B) Side view of wind tunnel system along with the acrylic port used to flux noni
1528 odor into the tunnel volume.
1529 (C) Comparison of mean trajectory ground speeds for the three genotypes
1530 studied.
1531 (D) Schematic of two plume models used to analyze data compared to the point
1532 cloud distribution of *D. sechellia* trajectories in the wind tunnel volume. A
1533 “straight” model (solid orange line) which is aligned in space with the odor port, or
1534 a “sloped” model (dashed orange line) for which the plume sinks by 5 cm from the
1535 odor port to the tunnel end.
1536 (E) Radial distance calculations comparing mean radial distance of points from
1537 the plume centerline considering either the sloped or straight plume model (left
1538 two plots). The same data is also shown without the restriction to limit this
1539 analysis to 10 cm above or below the plume’s altitude (right two plots).
1540 (F) Left, course direction distributions within a 3 cm radius of the plume centerline
1541 for either the sloped plume model (as in **Fig. 2G**) for the downwind and upwind

1542 halves of the wind tunnel, up to 5 cm downwind from the plume origin. Right, the
1543 same analysis assuming a straight plume model.

1544

1545 **Figure S5: Additional conditions of optogenetic stimulation.**

1546 **(A)** Optic fiber-mediated illumination of one antenna in the tethered fly. The photo
1547 was taken from below the apparatus.

1548 **(B)** Behavioral responses to optogenetic stimulation of Or22a/b OSNs in *D.*
1549 *melanogaster* using a *Gal4* knock-in line (see **Fig. 3A** for methodological details)
1550 Genotype: *D. melanogaster w;Or22a/b^{Gal4}/UAS-CsChrimson-Venus*. Left, time
1551 course of ΔWBA . Right, quantification within each phase. Paired *t*-test, $P > 0.05$.

1552 **(C)** Behavioral responses to optogenetic stimulation of effector control flies (*UAS-*
1553 *CsChrimson-Venus*) in *D. melanogaster* (left) and *D. sechellia* (right). Paired *t*-
1554 test, $P > 0.05$. Genotypes: *D. melanogaster w;+/UAS-CsChrimson-Venus*, *D.*
1555 *sechellia w;;;+/UAS-CsChrimson-Venus*.

1556 **(D)** Behavioral responses to optogenetic stimulation of Or22a OSNs in *D.*
1557 *sechellia* using *CsChrimson* by stimulating the left antenna induces leftward
1558 turning behavior (resulting in reduced ΔWBA values compared to control flies).
1559 Paired *t*-test, ** $P < 0.01$; * $P < 0.05$; otherwise $P > 0.05$. Genotype as in **Fig. 3A**.

1560

1561 **Figure S6: SPARC2 allows genetic manipulation of a subset of Or22a OSNs.**

1562 **(A)** Schematic illustrating the principle of SPARC2 (Isaacman-Beck et al., 2020).
1563 Top, $\Phi C31$ -mediated recombination leads to removal of a stop cassette flanked
1564 by attP sites. Co-expression of *Gal4* in the same cell leads to transcriptional
1565 activation of a reporter gene. Middle, recombination with an alternative attP site
1566 does not lead to a functional read-out. Depending on the attP version present in
1567 the cassette, recombination efficiencies vary (D, dense; I, intermediate; S,
1568 sparse). Bottom, after recombination, a proportion of *Gal4*-expressing cells – in
1569 this study Or22a OSNs – will express the respective SPARC2 transgene.

1570 **(B)** Left, immunofluorescence for GFP on whole-mount antennae from animals
1571 expressing different *SPARC2-X-GFP* versions in Or22a neurons. Right,
1572 quantification of the number of Or22a OSNs labelled by SPARC2 versions in *D.*
1573 *melanogaster*. Genotypes: *D. melanogaster nSyb- $\Phi C31$ /+;Or22a^{Gal4}/UAS-*
1574 *SPARC2-X-GFP*. The SPARC2-D transgene labelled ~50% of Or22a OSNs
1575 (compare with **Fig. 1C**) and was therefore used to generate transgenic constructs
1576 in *D. sechellia*.

1577 **(C)** Optogenetic stimulation of Or22a OSNs in *D. sechellia* using a lower light
1578 intensity. Electrophysiological measurements confirm that this light intensity
1579 evokes a similar degree of OSN firing as in the SPARC2-D-*CsChrimson*
1580 experiment. Paired *t*-test. * $P < 0.05$; otherwise $P > 0.05$. Electrophysiological
1581 data are re-plotted from **Fig. 3A**.

1582 **(D)** Immunofluorescence for HA and nc82 on a whole-mount brain of *D. sechellia*
1583 *Or22a^{Gal4}* transgenic flies expressing *UAS-SPARC2-D-TNT-HA-GeCO*, revealing
1584 selective strong expression in Or22a OSNs projecting to DM2. The white
1585 arrowheads point to a few cells (putative glia due to their apparent lack of
1586 processes) labelled in the central brain. Scale bar, 50 μ m.

1587

1588 **Figure S7: Whole-cell patch clamp recordings from VM5d PN.**

1589 **(A)** Voltage trace (top) and peri-stimulus time histogram (PSTH, bottom) of VM5d
1590 PN responses to a dilution series of 2-heptanone. Mean is shown for the voltage
1591 trace and mean \pm SEM are shown for the PSTH. $n = 2-5$ animals.

1592 **(B)** Start and end responses of VM5d PN to various dilutions of 2-heptanone.
1593 Quantification at the start (first 50 ms), end (last 500 ms before odor offset) and
1594 decay magnitude (start - end) spike frequencies are shown. Student's *t*-test. **P* <
1595 0.05. *n* = 2-5 animals (mean values and SEM for each concentration listed in
1596 **Supplemental Table 1**).
1597

1598 **Figure S8: Dose-response odor responses of OSNs and PNs in Or85b and**
1599 **Or22a pathways.**

1600 **(A-B)** Representative odor-evoked calcium responses in the axon termini of
1601 Or85b OSNs **(A)** and dendrites of VM5d PNs **(B)** in *D. melanogaster* and *D.*
1602 *sechellia*. Far left, schematic of the OSN-PN populations under investigation; the
1603 population subject to imaging analysis is shown in a darker color. Left,
1604 representative confocal images of the raw fluorescence of GaMP6f showing the
1605 plane used for imaging with glomerular labels; corresponding solvent and odor
1606 stimulus-induced fluorescent changes are also shown. Middle panels, time
1607 courses in response to solvents and two odor dilutions (mean ± SEM $\Delta F/F_0$, bars
1608 indicate the timing of stimulus). Right, quantifications of peak $\Delta F/F_0$ for a dilution
1609 series of each odor (Dunnett's test, control: solvent, *** *P* < 0.001; * *P* < 0.01; * *P*
1610 < 0.05; otherwise *P* > 0.05, *n* = 7 (*D. melanogaster* OSNs), 8 (*D. sechellia* OSNs),
1611 7 (*D. melanogaster* PNs), 6 (*D. sechellia* PNs) animals. Genotypes are indicated
1612 in **Fig. 5G** legend.

1613 **(C-D)** Representative odor-evoked calcium responses in the axon termini of
1614 Or22a OSNs **(C)** and DM2 PNs **(D)** in *D. melanogaster* and *D. sechellia*. *n* = 10
1615 animals each. Genotypes are indicated in **Fig. 5G** legend.

1616 **(E)** Calcium imaging of DM2 PNs following reintroduction of *DmelOr22a* or
1617 *DsecOr22a* in Or22a OSNs in *D. melanogaster* lacking endogenous receptor
1618 expression. Left, time courses of odor responses. Middle, quantifications of peak
1619 $\Delta F/F_0$ (Dunnett's test, control: solvent, *** *P* < 0.001; * *P* < 0.01; * *P* < 0.05;
1620 otherwise *P* > 0.05,). *n* = 7 animals each. Right, normalized GCaMP6f
1621 fluorescence changes. Genotypes: *D. melanogaster*
1622 *w;Or22a/b^{Gal4}/Or22a/b^{Gal4};UAS-DmelOr22a,VT033006-LexA/VT033006-*
1623 *LexA,LexAop-GCaMP6m* (*DmelOr22a* allele rescue),
1624 *w;Or22a/b^{Gal4}/Or22a/b^{Gal4};UAS-DsecOr22a,VT033006-LexA/VT033006-*
1625 *LexA,LexAop-GCaMP6m* (*DsecOr22a* allele rescue).
1626

1627 **Figure S9: Odor response reliability.**

1628 Odor response reliability of VM5d PNs. **(A-B)** Calcium responses of VM5d PNs in
1629 response to repeated stimulation with 2-heptanone (concentration (Log) indicated
1630 on the figure) in *D. melanogaster* **(A)** and *D. sechellia* **(B)**. Left, quantification of
1631 peak $\Delta F/F_0$ from eight trials of stimulation. Dunnett's test, compared to control
1632 (Trial 1). NS (*P* > 0.05). *n* = 8 animals each. Right, time courses of responses in
1633 trial 1 and 8 shown as mean ± SEM $\Delta F/F_0$. The odor stimulus (1 s) is shown with
1634 a black bar. **(C)** Quantification of mean, standard deviation and coefficient of
1635 variation of peak $\Delta F/F_0$ across the eight stimulation trials. Welch's *t*-test. NS (*P* >
1636 0.05).
1637

1638 **Figure S10: *D. sechellia* VM5d PNs show persistent response to long odor**
1639 **stimulation**

1640 Calcium responses of Or85b/VM5d neurons in response to long odor stimulation of
1641 *D. melanogaster* Or85b OSNs **(A)**, *D. melanogaster* VM5d PNs **(B)**, *D.*

1642 *sechellia* OSNs (C), and *D. sechellia* PNs (D). Left, time courses of the odor
1643 response (mean \pm SEM $\Delta F/F_0$). Bars indicate the timing of long odor stimulation
1644 (10 s). Right, maximum $\Delta F/F_0$ in the first and last 2.5 s time windows are
1645 compared. Paired *t*-test. ** $P < 0.01$; * $P < 0.05$. $n = 7$ (OSNs) or 8 (PNs) animals
1646 for both species. Genotypes are indicated in the **Fig. 5G** legend.

1647

1648 **Figure S11: Odor response sensitivity in control glomeruli.**

1649 Odor-evoked dose-dependent calcium responses in control glomeruli of *D.*
1650 *melanogaster* VA2 (Or92a) PNs (A), *D. sechellia* VA2 PNs (B), *D. melanogaster*
1651 DM4 (Or59b) PNs (C), and *D. sechellia* DM4 PNs (D). Left, time courses in
1652 response to solvents and specific odor dilutions (mean \pm SEM $\Delta F/F_0$, bars
1653 indicate the timing of stimuli). Right, quantifications of peak $\Delta F/F_0$ (Dunnett's test,
1654 control: solvent, *** $P < 0.001$; * $P < 0.01$; * $P < 0.05$; otherwise $P > 0.05$), $n = 7$
1655 each. The genotype for the VA2 and DM4 PN calcium imaging is the same as for
1656 DM2 PN imaging shown in **Fig. 5G**.

1657

1658 **Figure S12: Pharmacological manipulations of lateral inhibition.**

1659 (A,B) Odor pulse responses of VM5d PNs following application of a GABA_A (A,
1660 Picrotoxin) and GABA_B (B, CGP54626) antagonist. PN responses in normal AHL
1661 saline (left) or containing 100 μ M picrotoxin or 50 μ M CGP54626 (middle). The
1662 ratio between 10th and 1st odor pulses are shown on the far right. Paired *t*-test. **
1663 $P < 0.01$, * $P < 0.05$, NS $P > 0.05$. $n = 7$ animals each. Genotypes are indicated in
1664 **Fig. 5G** legend.

1665 c, Raw GCaMP fluorescence intensity in VM5d PNs in *D. melanogaster* (left) and
1666 *D. sechellia* (right) following GABA antagonist application. Mean fluorescence
1667 before (4-5 s; as "Baseline") and during (5-9 s; as "Odor") the stimulus was
1668 quantified. Paired *t*-test, ** $P < 0.01$, * $P < 0.05$, NS $P > 0.05$. $n = 8$ animals each.
1669 Genotype as in **Fig. 5G**.

1670

1671 **Figure S13: Variation in neuron numbers within and across species.**

1672 (A) Correlation between OSN number and synapse numbers across glomeruli
1673 from *D. melanogaster* OSN quantification (Grabe et al., 2016) and connectome
1674 (Schlegel et al., 2021) data. OSN outputs were quantified separately for
1675 connections to PNs (left), LNs (middle), and OSNs (right). *r* and *p* values are
1676 calculated by Pearson's correlation analysis.

1677 (B) Variation in basiconic sensilla neuron numbers in the *D. melanogaster*
1678 species subgroup. Numbers of Or42b, Or59b and Or22a/(b) neurons (housed in
1679 ab1, ab2 and ab3 sensilla, respectively) based on RNA FISH on whole-mount
1680 antennae across the *D. melanogaster* species subgroup; Ma, million years ago (n
1681 = 7-14, females). For strain details see **Supplemental Table 2**.

1682

1683

1684 **Supplemental Tables**

1685

1686 **Supplemental Table 1:** Spike counts for electrophysiological experiments.

1687

1688 **Supplemental Table 2:** Wild-type and transgenic lines used and generated in
1689 this study.

1690

1691 **Supplemental Table 3:** Oligonucleotides used to generate single sgRNA
1692 expression vectors and *in situ* probe templates.

1693

1694 **Supplemental Table 4:** Oligonucleotides used to generate multi-sgRNA
1695 expression vectors.

1696 **References**

1697

1698 Alvarez-Ocana, R., Shahandeh, M.P., Ray, V., Auer, T.O., Gompel, N., and
1699 Benton, R. (2023). Odor-regulated oviposition behavior in an ecological specialist.

1700 Nat Commun 14, 3041.

1701 Andolfatto, P., Davison, D., Erezyilmaz, D., Hu, T.T., Mast, J., Sunayama-Morita,
1702 T., and Stern, D.L. (2011). Multiplexed shotgun genotyping for rapid and efficient
1703 genetic mapping. Genome Research 21, 610-617.

1704 Arendt, D., Bertucci, P.Y., Achim, K., and Musser, J.M. (2019). Evolution of
1705 neuronal types and families. Curr Opin Neurobiol 56, 144-152.

1706 Arnoult, L., Su, K.F., Manoel, D., Minervino, C., Magrina, J., Gompel, N., and
1707 Prud'homme, B. (2013). Emergence and diversification of fly pigmentation
1708 through evolution of a gene regulatory module. Science 339, 1423-1426.

1709 Aso, Y., Sitaraman, D., Ichinose, T., Kaun, K.R., Vogt, K., Belliart-Guerin, G.,
1710 Placais, P.Y., Robie, A.A., Yamagata, N., Schnaitmann, C., et al. (2014).
1711 Mushroom body output neurons encode valence and guide memory-based action
1712 selection in *Drosophila*. Elife 3, e04580.

1713 Auer, T.O., Alvarez-Ocana, R., Cruchet, S., Benton, R., and Arguello, J.R. (2022).
1714 Copy number changes in co-expressed odorant receptor genes enable selection
1715 for sensory differences in drosophilid species. Nature ecology & evolution 6,
1716 1343-1353.

1717 Auer, T.O., Khallaf, M.A., Silbering, A.F., Zappia, G., Ellis, K., Alvarez-Ocana, R.,
1718 Arguello, J.R., Hansson, B.S., Jefferis, G.S.X.E., Caron, S.J.C., et al. (2020).
1719 Olfactory receptor and circuit evolution promote host specialization. Nature 579,
1720 402-408.

1721 Auer, T.O., Shahandeh, M.P., and Benton, R. (2021). *Drosophila sechellia*: A
1722 Genetic Model for Behavioral Evolution and Neuroecology. Annu Rev Genet 55,
1723 527-554.

1724 Backhaus, B., Sulkowski, E., and Schlote, F.W. (1984). A semi-synthetic general-
1725 purpose medium for *D. melanogaster*. Drosophila Information Service 60, 210-
1726 212.

1727 Badel, L., Ohta, K., Tsuchimoto, Y., and Kazama, H. (2016). Decoding of
1728 Context-Dependent Olfactory Behavior in *Drosophila*. Neuron 91, 155-167.

1729 Barish, S., and Volkan, P.C. (2015). Mechanisms of olfactory receptor neuron
1730 specification in *Drosophila*. Wiley interdisciplinary reviews Developmental biology
1731 4, 609-621.

1732 Benton, R. (2022). *Drosophila* olfaction: past, present and future. Proc Biol Sci
1733 289, 20222054.

1734 Bhandawat, V., Olsen, S.R., Gouwens, N.W., Schlieff, M.L., and Wilson, R.I.
1735 (2007). Sensory processing in the *Drosophila* antennal lobe increases reliability
1736 and separability of ensemble odor representations. Nat Neurosci 10, 1474-1482.

1737 Byk, T., Bar-Yaacov, M., Doza, Y.N., Minke, B., and Selinger, Z. (1993).
1738 Regulatory arrestin cycle secures the fidelity and maintenance of the fly
1739 photoreceptor cell. Proceedings of the National Academy of Sciences of the
1740 United States of America 90, 1907-1911.

1741 Catania, K.C. (1995). A comparison of the Eimer's organs of three North
1742 American moles: the hairy-tailed mole (*Parascalops breweri*), the star-nosed mole
1743 (*Condylura cristata*), and the eastern mole (*Scalopus aquaticus*). J Comp Neurol
1744 354, 150-160.

- 1745 Chai, P.C., Cruchet, S., Wigger, L., and Benton, R. (2019). Sensory neuron
1746 lineage mapping and manipulation in the *Drosophila* olfactory system. *Nat*
1747 *Commun* 10, 643.
- 1748 Chou, Y.H., Spletter, M.L., Yaksi, E., Leong, J.C., Wilson, R.I., and Luo, L.
1749 (2010). Diversity and wiring variability of olfactory local interneurons in the
1750 *Drosophila* antennal lobe. *Nat Neurosci* 13, 439-449.
- 1751 Couto, A., Alenius, M., and Dickson, B.J. (2005). Molecular, anatomical, and
1752 functional organization of the *Drosophila* olfactory system. *Curr Biol* 15, 1535-
1753 1547.
- 1754 de Bruyne, M., Smart, R., Zammit, E., and Warr, C.G. (2010). Functional and
1755 molecular evolution of olfactory neurons and receptors for aliphatic esters across
1756 the *Drosophila* genus. *J Comp Physiol A Neuroethol Sens Neural Behav Physiol*
1757 196, 97-109.
- 1758 Dekker, T., Ibba, I., Siju, K.P., Stensmyr, M.C., and Hansson, B.S. (2006).
1759 Olfactory shifts parallel superspecialism for toxic fruit in *Drosophila melanogaster*
1760 sibling, *D. sechellia*. *Curr Biol* 16, 101-109.
- 1761 Elkahlah, N.A., Rogow, J.A., Ahmed, M., and Clowney, E.J. (2020). Presynaptic
1762 developmental plasticity allows robust sparse wiring of the *Drosophila* mushroom
1763 body. *Elife* 9, e52278.
- 1764 Ellis, K.E., Smihula, H., Ganguly, I., Vigato, E., Bervoets, S., Auer, T.O., Benton,
1765 R., Litwin-Kumar, A., and Caron, S.J.C. (2023). Evolution of connectivity
1766 architecture in the *Drosophila* mushroom body. *bioRxiv*,
1767 doi:10.1101/2023.1102.1110.528036.
- 1768 Gaudry, Q., Hong, E.J., Kain, J., de Bivort, B.L., and Wilson, R.I. (2013).
1769 Asymmetric neurotransmitter release enables rapid odor lateralization in
1770 *Drosophila*. *Nature* 493, 424-428.
- 1771 Godfrey, R.K., and Gronenberg, W. (2019). Brain evolution in social insects:
1772 advocating for the comparative approach. *J Comp Physiol A Neuroethol Sens*
1773 *Neural Behav Physiol* 205, 13-32.
- 1774 Gohl, D.M., Silies, M.A., Gao, X.J., Bhalerao, S., Luongo, F.J., Lin, C.C., Potter,
1775 C.J., and Clandinin, T.R. (2011). A versatile in vivo system for directed dissection
1776 of gene expression patterns. *Nature methods* 8, 231-237.
- 1777 Grabe, V., Baschwitz, A., Dweck, H.K.M., Lavista-Llanos, S., Hansson, B.S., and
1778 Sachse, S. (2016). Elucidating the Neuronal Architecture of Olfactory Glomeruli in
1779 the *Drosophila* Antennal Lobe. *Cell Rep* 16, 3401-3413.
- 1780 Gratz, S.J., Ukken, F.P., Rubinstein, C.D., Thiede, G., Donohue, L.K., Cummings,
1781 A.M., and O'Connor-Giles, K.M. (2014). Highly specific and efficient
1782 CRISPR/Cas9-catalyzed homology-directed repair in *Drosophila*. *Genetics* 196,
1783 961-971.
- 1784 Gratz, S.J., Wildonger, J., Harrison, M.M., and O'Connor-Giles, K.M. (2013).
1785 CRISPR/Cas9-mediated genome engineering and the promise of designer flies
1786 on demand. *Fly* 7.
- 1787 Gupta, B.P., Flores, G.V., Banerjee, U., and Rodrigues, V. (1998). Patterning an
1788 epidermal field: *Drosophila* lozenge, a member of the AML-1/Runt family of
1789 transcription factors, specifies olfactory sense organ type in a dose-dependent
1790 manner. *Dev Biol* 203, 400-411.
- 1791 Hansson, B.S., and Stensmyr, M.C. (2011). Evolution of insect olfaction. *Neuron*
1792 72, 698-711.
- 1793 Herculano-Houzel, S. (2011). Not all brains are made the same: new views on
1794 brain scaling in evolution. *Brain Behav Evol* 78, 22-36.

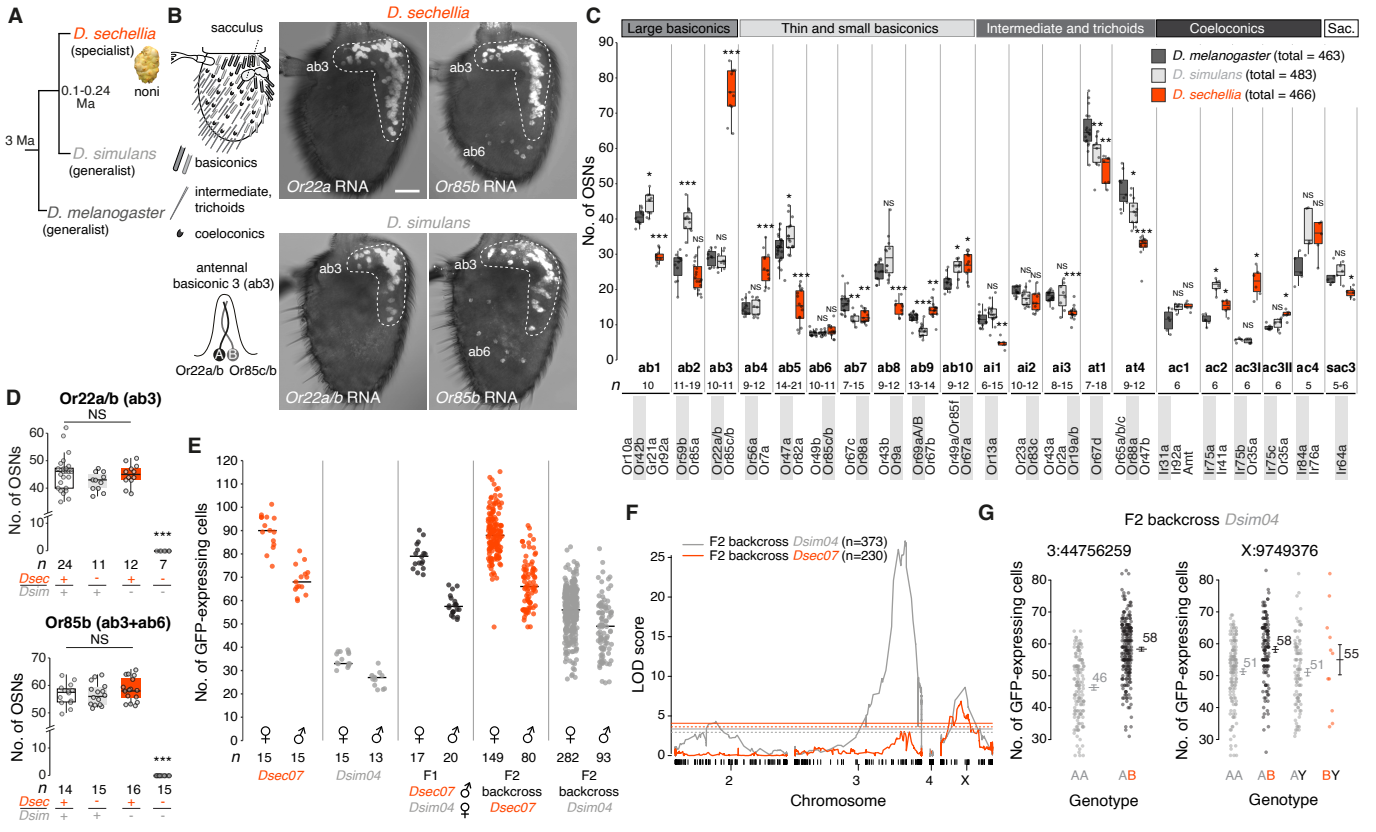
- 1795 Horn, C., and Wimmer, E.A. (2000). A versatile vector set for animal
1796 transgenesis. *Dev Genes Evol* 210, 630-637.
- 1797 Huang, J., Zhang, W., Qiao, W., Hu, A., and Wang, Z. (2010). Functional
1798 connectivity and selective odor responses of excitatory local interneurons in
1799 *Drosophila* antennal lobe. *Neuron* 67, 1021-1033.
- 1800 Ibba, I., Angioy, A.M., Hansson, B.S., and Dekker, T. (2010). Macroglomeruli for
1801 fruit odors change blend preference in *Drosophila*. *Die Naturwissenschaften* 97,
1802 1059-1066.
- 1803 Isaacman-Beck, J., Paik, K.C., Wienecke, C.F.R., Yang, H.H., Fisher, Y.E.,
1804 Wang, I.E., Ishida, I.G., Maimon, G., Wilson, R.I., and Clandinin, T.R. (2020).
1805 SPARC enables genetic manipulation of precise proportions of cells. *Nat*
1806 *Neurosci* 23, 1168-1175.
- 1807 Jeanne, J.M., and Wilson, R.I. (2015). Convergence, Divergence, and
1808 Reconvergence in a Feedforward Network Improves Neural Speed and Accuracy.
1809 *Neuron* 88, 1014-1026.
- 1810 Jones, C.D. (2005). The genetics of adaptation in *Drosophila sechellia*. *Genetica*
1811 123, 137-145.
- 1812 Kazama, H., and Wilson, R.I. (2008). Homeostatic matching and nonlinear
1813 amplification at identified central synapses. *Neuron* 58, 401-413.
- 1814 Keeseey, I.W., Zhang, J., Depetris-Chauvin, A., Obiero, G.F., Gupta, A., Gupta, N.,
1815 Vogel, H., Knaden, M., and Hansson, B.S. (2022). Functional olfactory evolution
1816 in *Drosophila suzukii* and the subgenus *Sophophora*. *iScience* 25, 104212.
- 1817 Klapoetke, N.C., Murata, Y., Kim, S.S., Pulver, S.R., Birdsey-Benson, A., Cho,
1818 Y.K., Morimoto, T.K., Chuong, A.S., Carpenter, E.J., Tian, Z., *et al.* (2014).
1819 Independent optical excitation of distinct neural populations. *Nat Methods* 11,
1820 338-346.
- 1821 Kudo, K., Shiraishi, J., Nishimura, S., Bungo, T., and Tabata, S. (2010). The
1822 number of taste buds is related to bitter taste sensitivity in layer and broiler
1823 chickens. *Anim Sci J* 81, 240-244.
- 1824 Leal, W.S. (2013). Odorant reception in insects: roles of receptors, binding
1825 proteins, and degrading enzymes. *Annu Rev Entomol* 58, 373-391.
- 1826 Lee, D., and Benton, R. (2023). Comparative single-cell transcriptomic atlases
1827 reveal conserved and divergent features of drosophilid central brains. *bioRxiv*,
1828 doi:10.1101/2023.1111.1122.568274.
- 1829 Leiss, F., Koper, E., Hein, I., Fouquet, W., Lindner, J., Sigrist, S., and Tavosanis,
1830 G. (2009). Characterization of dendritic spines in the *Drosophila* central nervous
1831 system. *Dev Neurobiol* 69, 221-234.
- 1832 Li, H., Li, T., Horns, F., Li, J., Xie, Q., Xu, C., Wu, B., Keschull, J.M.,
1833 McLaughlin, C.N., Kolluru, S.S., *et al.* (2020). Single-Cell Transcriptomes Reveal
1834 Diverse Regulatory Strategies for Olfactory Receptor Expression and Axon
1835 Targeting. *Curr Biol* 30, 1189-1198 e1185.
- 1836 Linz, J., Baschwitz, A., Strutz, A., Dweck, H.K., Sachse, S., Hansson, B.S., and
1837 Stensmyr, M.C. (2013). Host plant-driven sensory specialization in *Drosophila*
1838 *erecta*. *Proceedings Biological sciences / The Royal Society* 280, 20130626.
- 1839 Liu, W.W., and Wilson, R.I. (2013). Glutamate is an inhibitory neurotransmitter in
1840 the *Drosophila* olfactory system. *Proceedings of the National Academy of*
1841 *Sciences of the United States of America* 110, 10294-10299.
- 1842 Meisami, E. (1989). A proposed relationship between increases in the number of
1843 olfactory receptor neurons, convergence ratio and sensitivity in the developing
1844 rat. *Brain research Developmental brain research* 46, 9-19.

- 1845 Mosca, T.J., Luginbuhl, D.J., Wang, I.E., and Luo, L. (2017). Presynaptic LRP4
1846 promotes synapse number and function of excitatory CNS neurons. *Elife* 6,
1847 e27347.
- 1848 Mosca, T.J., and Luo, L. (2014). Synaptic organization of the antennal lobe and
1849 its regulation by the Teneurins. *Elife* 3, e03726.
- 1850 Nagel, K.I., Hong, E.J., and Wilson, R.I. (2015). Synaptic and circuit mechanisms
1851 promoting broadband transmission of olfactory stimulus dynamics. *Nat Neurosci*
1852 18, 56-65.
- 1853 O'Mahony, M. (1986). Sensory Adaptation. *Journal of Sensory Studies* 1, 237-
1854 258.
- 1855 Olsen, S.R., Bhandawat, V., and Wilson, R.I. (2010). Divisive normalization in
1856 olfactory population codes. *Neuron* 66, 287-299.
- 1857 Pan, J.W., Li, Q., Barish, S., Okuwa, S., Zhao, S., Soeder, C., Kanke, M., Jones,
1858 C.D., and Volkan, P.C. (2017). Patterns of transcriptional parallelism and variation
1859 in the developing olfactory system of *Drosophila* species. *Sci Rep* 7, 8804.
- 1860 Peichl, L. (2005). Diversity of mammalian photoreceptor properties: adaptations
1861 to habitat and lifestyle? *Anat Rec A Discov Mol Cell Evol Biol* 287, 1001-1012.
- 1862 Picelli, S., Bjorklund, A.K., Reinius, B., Sagasser, S., Winberg, G., and Sandberg,
1863 R. (2014). Tn5 transposase and tagmentation procedures for massively scaled
1864 sequencing projects. *Genome Res* 24, 2033-2040.
- 1865 Port, F., and Bullock, S.L. (2016). Augmenting CRISPR applications in *Drosophila*
1866 with tRNA-flanked sgRNAs. *Nat Methods* 13, 852-854.
- 1867 Port, F., Chen, H.M., Lee, T., and Bullock, S.L. (2014). Optimized CRISPR/Cas
1868 tools for efficient germline and somatic genome engineering in *Drosophila*.
1869 *Proceedings of the National Academy of Sciences of the United States of*
1870 *America* 111, E2967-2976.
- 1871 Prieto-Godino, L.L., Rytz, R., Cruchet, S., Bargeton, B., Abuin, L., Silbering, A.F.,
1872 Ruta, V., Dal Peraro, M., and Benton, R. (2017). Evolution of Acid-Sensing
1873 Olfactory Circuits in Drosophilids. *Neuron* 93, 661-676.
- 1874 Prieto-Godino, L.L., Schmidt, H.R., and Benton, R. (2021). Molecular
1875 reconstruction of recurrent evolutionary switching in olfactory receptor specificity.
1876 *Elife* 10, e69732.
- 1877 Roberts, R.J.V., Pop, S., and Prieto-Godino, L.L. (2022). Evolution of central
1878 neural circuits: state of the art and perspectives. *Nat Rev Neurosci* 23, 725-743.
- 1879 Saina, M., and Benton, R. (2013). Visualizing olfactory receptor expression and
1880 localization in *Drosophila*. *Methods in Molecular Biology* 1003, 211-228.
- 1881 Sanchez-Alcaniz, J.A., Zappia, G., Marion-Poll, F., and Benton, R. (2017). A
1882 mechanosensory receptor required for food texture detection in *Drosophila*. *Nat*
1883 *Commun* 8, 14192.
- 1884 Schindelin, J., Arganda-Carreras, I., Frise, E., Kaynig, V., Longair, M., Pietzsch,
1885 T., Preibisch, S., Rueden, C., Saalfeld, S., Schmid, B., *et al.* (2012). Fiji: an open-
1886 source platform for biological-image analysis. *Nat Methods* 9, 676-682.
- 1887 Schlegel, P., Bates, A.S., Sturner, T., Jagannathan, S.R., Drummond, N., Hsu, J.,
1888 Serratos Capdevila, L., Javier, A., Marin, E.C., Barth-Maron, A., *et al.* (2021).
1889 Information flow, cell types and stereotypy in a full olfactory connectome. *Elife* 10,
1890 e66018.
- 1891 Serences, J.T. (2011). Mechanisms of selective attention: response
1892 enhancement, noise reduction, and efficient pooling of sensory responses.
1893 *Neuron* 72, 685-687.

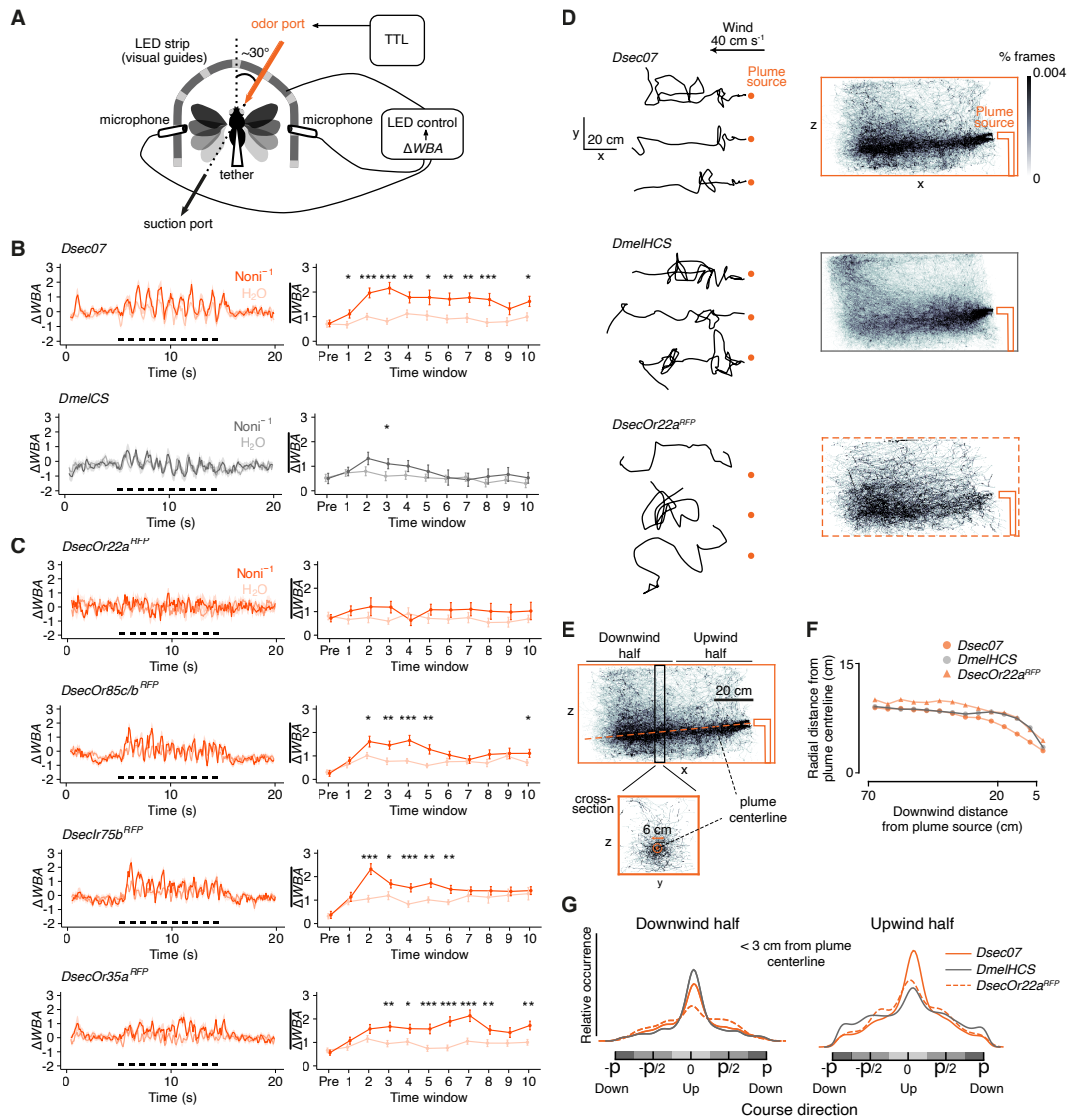
- 1894 Silbering, A.F., Bell, R., Galizia, C.G., and Benton, R. (2012). Calcium imaging of
1895 odor-evoked responses in the *Drosophila* antennal lobe. *Journal of Vis Exp*, doi:
1896 10.3791/2976.
- 1897 Silbering, A.F., Rytz, R., Grosjean, Y., Abuin, L., Ramdya, P., Jefferis, G.S., and
1898 Benton, R. (2011). Complementary Function and Integrated Wiring of the
1899 Evolutionarily Distinct *Drosophila* Olfactory Subsystems. *The Journal of*
1900 *Neuroscience* 31, 13357-13375.
- 1901 Stensmyr, M.C. (2009). *Drosophila sechellia* as a model in chemosensory
1902 neuroecology. *Ann N Y Acad Sci* 1170, 468-475.
- 1903 Stensmyr, M.C., Dekker, T., and Hansson, B.S. (2003). Evolution of the olfactory
1904 code in the *Drosophila melanogaster* subgroup. *Proc Biol Sci* 270, 2333-2340.
- 1905 Stern, D.L. (2017). Tagmentation-Based Mapping (TagMap) of Mobile DNA
1906 Genomic Insertion Sites. bioRxiv, 037762.
- 1907 Stern, D.L., Crocker, J., Ding, Y., Frankel, N., Kappes, G., Kim, E., Kuzmickas,
1908 R., Lemire, A., Mast, J.D., and Picard, S. (2017). Genetic and Transgenic
1909 Reagents for *Drosophila simulans*, *D. mauritiana*, *D. yakuba*, *D. santomea* and *D.*
1910 *virilis*. *G3 (Bethesda)* 7, 1339-1347.
- 1911 Straw, A.D., Branson, K., Neumann, T.R., and Dickinson, M.H. (2011). Multi-
1912 camera real-time three-dimensional tracking of multiple flying animals. *J R Soc*
1913 *Interface* 8, 395-409.
- 1914 Talay, M., Richman, E.B., Snell, N.J., Hartmann, G.G., Fisher, J.D., Sorkac, A.,
1915 Santoyo, J.F., Chou-Freed, C., Nair, N., Johnson, M., *et al.* (2017). Transsynaptic
1916 Mapping of Second-Order Taste Neurons in Flies by *trans*-Tango. *Neuron* 96,
1917 783-795 e784.
- 1918 Thevenaz, P., Ruttimann, U.E., and Unser, M. (1998). A pyramid approach to
1919 subpixel registration based on intensity. *IEEE Trans Image Process* 7, 27-41.
- 1920 Tirian, L., and Dickson, B.J. (2017). The VT GAL4, LexA, and split-GAL4 driver
1921 line collections for targeted expression in the *Drosophila* nervous system. bioRxiv.
- 1922 Tobin, W.F., Wilson, R.I., and Lee, W.A. (2017). Wiring variations that enable and
1923 constrain neural computation in a sensory microcircuit. *Elife* 6, e24838.
- 1924 Turner, G.C., Bazhenov, M., and Laurent, G. (2008). Olfactory representations by
1925 *Drosophila* mushroom body neurons. *J Neurophysiol* 99, 734-746.
- 1926 van Breugel, F., and Dickinson, M.H. (2014). Plume-tracking behavior of flying
1927 *Drosophila* emerges from a set of distinct sensory-motor reflexes. *Curr Biol* 24,
1928 274-286.
- 1929 Vosshall, L.B., Wong, A.M., and Axel, R. (2000). An olfactory sensory map in the
1930 fly brain. *Cell* 102, 147-159.
- 1931 Wagh, D.A., Rasse, T.M., Asan, E., Hofbauer, A., Schwenkert, I., Durrbeck, H.,
1932 Buchner, S., Dabauvalle, M.C., Schmidt, M., Qin, G., *et al.* (2006). Bruchpilot, a
1933 protein with homology to ELKS/CAST, is required for structural integrity and
1934 function of synaptic active zones in *Drosophila*. *Neuron* 49, 833-844.
- 1935 Williams, R.W., and Herrup, K. (1988). The control of neuron number. *Annu Rev*
1936 *Neurosci* 11, 423-453.
- 1937 Wilson, R.I. (2013). Early olfactory processing in *Drosophila*: mechanisms and
1938 principles. *Annual review of neuroscience* 36, 217-241.
- 1939 Wilson, R.I., and Laurent, G. (2005). Role of GABAergic inhibition in shaping
1940 odor-evoked spatiotemporal patterns in the *Drosophila* antennal lobe. *J Neurosci*
1941 25, 9069-9079.

1942 Yan, H., Jafari, S., Pask, G., Zhou, X., Reinberg, D., and Desplan, C. (2020).
1943 Evolution, developmental expression and function of odorant receptors in insects.
1944 J Exp Biol 223, jeb208215.
1945

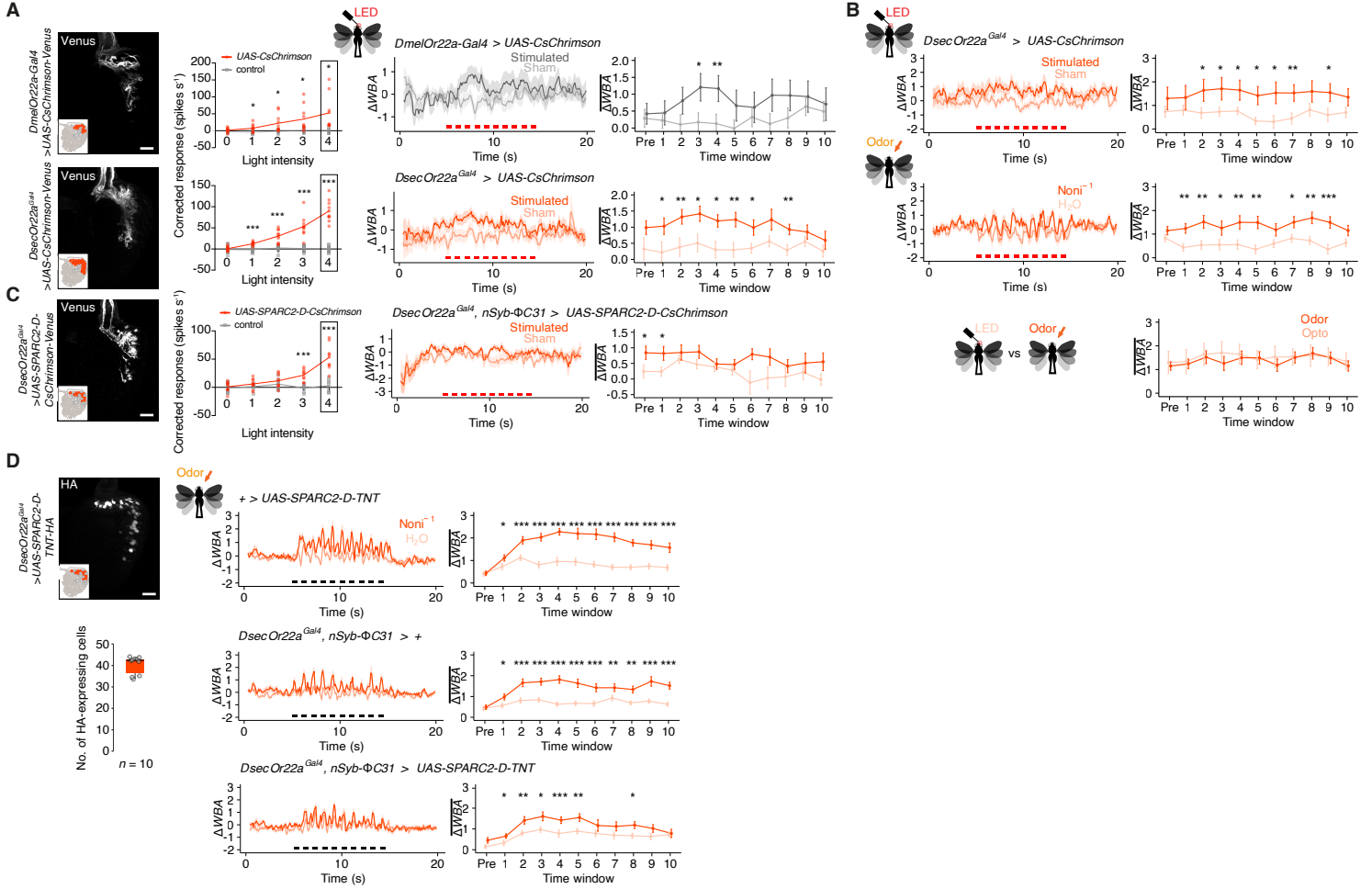
bioRxiv preprint doi: <https://doi.org/10.1101/2023.09.15.556782>; this version posted February 28, 2024. The copyright holder for this preprint (which was not certified by peer review) is the author/funder. All rights reserved. No reuse allowed without permission.



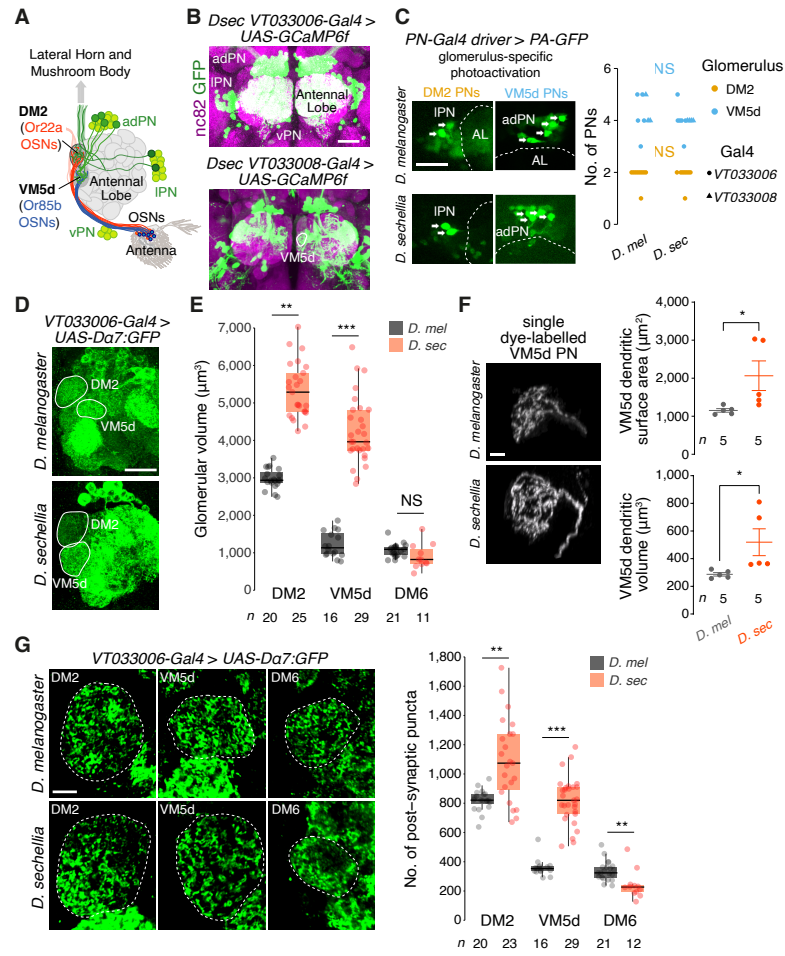
bioRxiv preprint doi: <https://doi.org/10.1101/2023.09.15.556782>; this version posted February 28, 2024. The copyright holder for this preprint (which was not certified by peer review) is the author/funder. All rights reserved. No reuse allowed without permission.



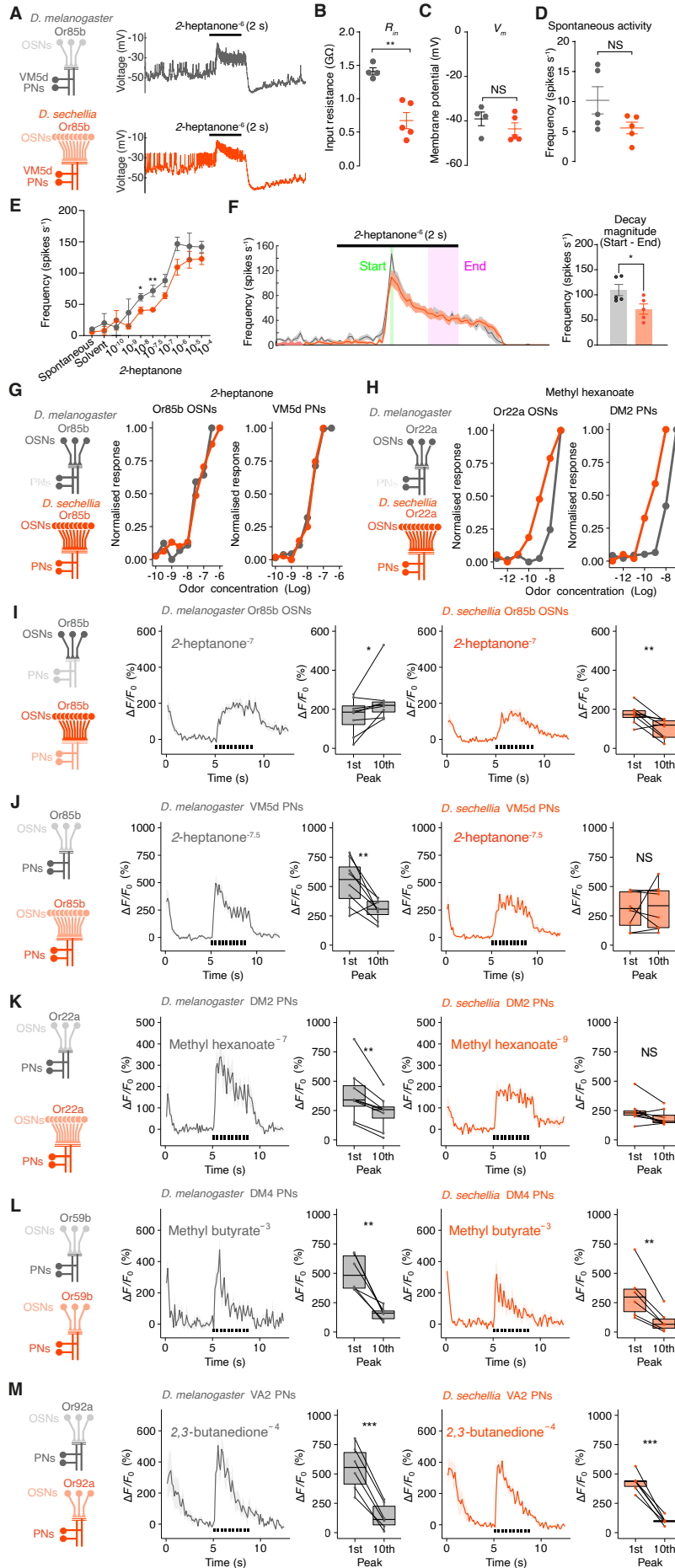
bioRxiv preprint doi: <https://doi.org/10.1101/2023.09.15.556782>; this version posted February 28, 2024. The copyright holder for this preprint (which was not certified by peer review) is the author/funder. All rights reserved. No reuse allowed without permission.



bioRxiv preprint doi: <https://doi.org/10.1101/2023.09.15.556782>; this version posted February 28, 2024. The copyright holder for this preprint (which was not certified by peer review) is the author/funder. All rights reserved. No reuse allowed without permission.



bioRxiv preprint doi: <https://doi.org/10.1101/2023.09.15.556782>; this version posted February 28, 2024. The copyright holder for this preprint (which was not certified by peer review) is the author/funder. All rights reserved. No reuse allowed without permission.



bioRxiv preprint doi: <https://doi.org/10.1101/2023.09.15.556782>; this version posted February 28, 2024. The copyright holder for this preprint (which was not certified by peer review) is the author/funder. All rights reserved. No reuse allowed without permission.

